Constrained Aerodynamic Shape Optimisation of the Flying V Outer Wing

van Luijk, N.L.M.; Vos, Roelof

Important note
To cite this publication, please use the final published version (if applicable).
Please check the document version above.

Constrained Aerodynamic Shape Optimisation of the Flying V Outer Wing

Nikki van Luijk* and Roelof Vos[†]

Delft University of Technology, 2629HS Delft, The Netherlands

The Flying V is a flying wing aircraft consisting of two pressurised passenger cabins placed in a V shape. Its longitudinal and lateral control is ensured via elevons and split flaps on the outboard wing, and rudders on the tip-mounted winglets. The goal of this study is to devise a design for the outboard wing of the Flying V through a constrained aerodynamic shape optimisation at cruise conditions. The design process is divided into a geometry preparation phase in which the existing parametrisation is adjusted, followed by a planform design optimisation guided by the Differential Evolution algorithm making use of a vortex-lattice method and an Euler flow analysis. The cross-sectional shape of the wing is subsequently optimised through a Free-Form Deformation (FFD) shape optimisation based on the Euler equations. Two FFD optimisations are conducted to evaluate the effect of the integration of the elevons. The highest lift-to-drag ratio is obtained by neglecting the control surface integration and amounts to 20.3. While the constraints related to this elevon integration reduce the efficiency to 19.4. The overall efficiency gain compared to the original aircraft design is equivalent to 13% and 8%, respectively. A further increase is expected once the inefficient outboard wing is optimised in more detail.

Nomenclature

AR	Aspect ratio [-]		S_{wet}	Wetted surface area [m^2]
b	Semi-wing span [m]		t/c	Thickness-to-chord ratio [-]
C_D	Drag coefficient [-]		$\bar{x}$	Design vector [-]
C_{D_0}	Zero lift drag coefficient [-]		y^+	Non-dimensional first layer height [-]
C_{D_f}	Friction drag coefficient [-]		α	Angle of attack [°]
$C_{D\text{inv}}$	Inviscid drag coefficient [-]		δ	Orientation angle of section 4 [°]
C_{D_P}	Pressure drag coefficient [-]		δs	Hinge line offset [m]
C_f	Friction coefficient in x direction [-]		ϵ_5	Incidence angle section 5 [°]
C_L	Lift coefficient [-]		η	Spanwise location [-]
C_m	Moment coefficient [-]		Λ	Leading edge sweep angle [°]
C_P	Pressure coefficient [-]		λ	Taper ratio [-]
C_P^*	Critical pressure coefficient [-]		μ	Torus angle [°]
c	Chord length [m]			
$\bar{c}$	Mean aerodynamic chord [m]		**Subscripts**	
E	Normalised lift distribution [-]		con.	Control surface
e	Oswald efficiency factor [-]		in	Inboard
f	Form factor [-]		loc.	Local
L_4	Leading edge kink position [m]		out	Outboard
M	Mach number [-]		r	Root
Re	Reynolds number [-]		t	Tip
S	Surface area [m^2]		0	Initial
S_{ref}	Wing reference area [m^2]			

*MSc student, Faculty of Aerospace Engineering, Kluyverweg 1, 2629HS Delft, the Netherlands.

[†]Associate Professor, Faculty of Aerospace Engineering, Kluyverweg 1, 2629HS Delft, the Netherlands, Associate Fellow AIAA.

I. Introduction

From the start of the commercial aviation era with wooden aircraft, up to and including the fly-by-wire composite aircraft that are here today, one trend can be observed: the tube-wing configuration has dominated the sky over the past 70 years. Tremendous efforts have been undertaken to improve the performance of these aircraft in all aspects. Developments in the power-plant, avionics, and aerodynamic design for example have doubled the efficiency of modern-day airliners compared to passenger aircraft five decades ago [1]. Nonetheless, it seems that a plateau has been reached in terms of efficiency with the latest aircraft, the Boeing 787 and Airbus A350. More advancements in the different areas of aircraft design and construction cannot double the efficiency of the tube-wing aircraft yet again [2]. Nevertheless, the pressure of making the aviation sector more efficient and thereby environmentally sustainable increases significantly; both the general public and political establishment demand action * †. Moreover, the aviation sector is expected to grow exponentially after recovering from the COVID-19 pandemic, while the constraints on noise, pollution, and environmental impact are tightened ‡. Hence new solutions need to be found.

Several studies conducted by Qin et al. put forward the flying wing and blended wing body configurations as possible solutions to the sustainability problem [3–5]. These configurations have the potential to reduce the fuel consumption per seat-kilometre. This is ascribed to the reduction in wetted area per unit volume due to the blending of the aerodynamic shape, structural components, and the payload bay. Additionally, these types of aircraft do not require high lift devices during take-off and landing, reducing noise pollution as well [1, 6]. While the concept of flying wings and blended wing bodies has been around for more than a century, the application of these configurations for passenger aircraft is still considered rare. The first recorded flight of a tailless aircraft already took place in 1911 with the D-8 tailless biplane developed by John Dunne [2, 7]. Thenceforth, developments in unconventional aircraft configurations advanced thanks to pioneers such as Alexander Lippisch, who built the very first delta wing aircraft [8]. These discoveries led to the well-known Aérospatiale-BAC Concorde passenger aircraft, and its Russian counterpart the Tupolev Tu-144. To this day, these remain the only tailless passenger aircraft. On the contrary, various military fighter aircraft were designed according to the flying wing or tailless aircraft principle, with the prime example being the Northrop Grumman B-2 Spirit Bomber [6].

Before the commercial aviation market can also widely make use of the advantages of blended wing bodies and flying wings, it must first overcome the challenges associated with these types of passenger aircraft. Stability and controllability issues limit the aircraft to be only viable in cruise, and the weight of a non-circular fuselage are merely examples of the issues faced [6]. Attempts were made by Qin et al. to develop the aerodynamic design of a blended wing body for the MOB project (a multi-disciplinary design optimisation study for blended wing bodies). The research included multi-disciplinary constraints and a multi-fidelity aerodynamic model consisting of a low-fidelity panel method, a high-fidelity Reynolds Averaged Navier Stokes Equations (RANS) model to resolve the boundary layer, followed by the Euler equations [3, 5]. Lyu and Martins took a different approach using a single-fidelity aerodynamic model based on the RANS equations in combination with a gradient-based optimisation algorithm [9]. A similar procedure was adopted by Reist et al. when investigating the aerodynamic design optimisation of a hybrid blended wing body [10]. A gradient-free optimisation approach was proven to also be feasible by Staub et al. when they performed an aerodynamic trade study on a blended wing body using a low fidelity panel method and a genetic algorithm [11].

Benad also saw the potential of blended wing bodies and flying wings and developed together with the Future Project Office (FPO) at Airbus GmbH the Flying V aircraft. According to Benad, the idea of the Flying V is "....to arrange two cylindrical pressurized sections for the payload swept back in the shape of a V and place them inside the front section of a wing with the same sweep angle" [6]. This results in the configuration shown in figure 1. To ensure both lateral and longitudinal control, elevons and split flaps are located on the outboard wing, while directional control is ensured by the rudders located on the winglets. This design aims to develop an aircraft with the highest possible lift-to-drag ratio which is competitive with the current state-of-the-art long-haul aircraft like the Airbus A350 [6]. This objective also means that similar top-level requirements are imposed: 361 passengers at a cruise Mach number of 0.85 with a nominal range of 14,350 km and a service ceiling of 13 km. To investigate the potential efficiency gain of the Flying V configuration, Faggiano performed a two-step multi-fidelity aerodynamic shape optimisation on the developed parametrisation [12]. A vortex lattice method was employed to explore the design space after which a genetic algorithm was used in combination with an Euler flow solver augmented with an empirical viscous drag module. This resulted in the estimate of a 25% higher aerodynamic efficiency as compared to NASA's Common Research Model (CRM) [12].

---

*NATS Aviation index 2020, Retrieved on 25-04-2022 from `https://www.nats.aero/features/aviation-index-2020/`

†Destination 2050, Retrieved on 25-04-2022 from `https://www.destination2050.eu`

‡Economic Impacts of COVID-19 on Civil Aviation, Retrieved on 25-04-2022 from `https://www.icao.int/sustainability`
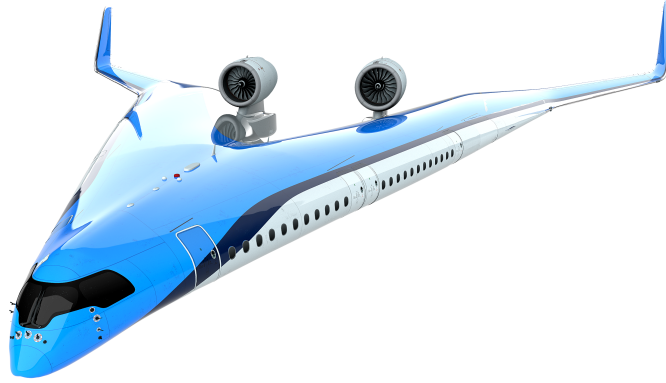
Fig. 1 Artist impression of the Flying V aircraft.

Throughout the years, the aircraft was investigated more in-depth to develop a design which satisfied constraints other than merely aerodynamic aspects. In this regard, van der Pluijm and Brouwer investigated the cockpit and centre-body fairing integration to incorporate pilot and systems integration requirements [13, 14]. Van der Pluijm devised a parametrisation for the cockpit and centre-body and subsequently utilised a similar aerodynamic model as Faggiano [13]. Brouwer took the resulting design as the starting point after which an updated parametrisation was developed. Furthermore, the higher-fidelity RANS flow model was used to investigate the aerodynamic aspects of the design, resulting in a 3.3% drag reduction compared to Fagginao's centre body design [14]. Concurrently, the effect of the winglet design on lateral-directional stability and control was analysed by Horwitz. Following the investigation's main objective, a low-fidelity vorticity-based 3D Panel method was chosen as the aerodynamic model [15]. A similar approach was taken by Oosterom in devising the conceptual family design of the Flying V. A multi-objective optimisation was performed in which also the aerodynamic performance was assessed. As the main goal of the analysis was not hard aerodynamic proof, a low-fidelity panel method was used [16]. Simultaneously, Hillen developed a new parametrisation of the Flying V intending to make it structurally efficient. The resulting (non-optimised) design was analysed using the aerodynamic module of Faggiano, resulting in a 13% lower lift-to-drag ratio than the initial aerodynamically optimised design [17].

The question that thus remains is: What is the maximal lift-to-drag ratio of the Flying V when considering the structurally efficient parametrisation and relevant multi-disciplinary constraints? Therefore, the goal of the presented study is to perform a constrained aerodynamic shape optimisation of the Flying V and assess its aerodynamic performance in design conditions. The current study is limited to the design optimisation of the outboard wing as the design of the inboard wing is dictated by the passenger cabin and structures rather than aerodynamic grounds. Furthermore, the outboard wing of Hillen experiences strong shock waves which need to be mitigated. To determine the optimised aerodynamic efficiency of the aircraft, it is required to discuss several sub-questions: how can the limitations of the current geometric and aerodynamic model be resolved, which aerodynamic analysis method is the most suitable for this application, and what are the relevant constraints and their effect on the resulting design?

The paper is structured as follows. First, the design strategy and methodology are presented in Section II. Section III covers the verification and validation of the chosen aerodynamic analysis method to demonstrate its validity. Subsequently, Section IV presents the five different designs for the outer wing of the Flying V and discusses the aerodynamic performance of each. At last, conclusions are drawn and recommendations for future studies are made in Section V.

## II. Design Strategy & Methodology

The parametric design of the Flying V was established in earlier conducted studies as discussed in Section I. This design is implemented using the ParaPy platform: a Knowledge-Based Engineering (KBE) Python-based framework which enables the automation of repetitive engineering tasks [§]. The parametric model of the aircraft is generated by the implemented Multi-Model Generator (MMG) following a multi-level parametrisation and a small number of

---

[§]ParaPy - Knowledge Based Engineering Platform, Retrieved on 29-04-2022 from `https://www.parapy.nl/`

user-defined inputs. The MMG relies on pre-existing classes offered by the ParaPy platform to generate the geometry of the aircraft. Next to pre-existing classes, several Application Programming Interfaces (APIs) are available through ParaPy as well. These include an API for Salome Mesh [¶], which automates the generation of unstructured meshes based on geometry built using ParaPy, and an interface with Stanford University Unstructured (SU2) [‖], a software offering multi-physics simulations. The applicability within ParaPy and its capabilities are important guidelines in the development of the geometric and aerodynamic model of the Flying V. The first step of the model development is to adjust the pre-existing parametric model to make it suitable for the optimisation process. This process is described in Section II.A. Subsequently, the aerodynamic design strategy in which this geometric model is used is outlined in Section II.B. The section is concluded with a description of the aerodynamic model in Section II.C.

A. Geometric Model Development

The Flying V parametric model developed by Hillen [17] serves as the starting point for the geometric model developed in this study. The parametrisation is generated to be structurally efficient in terms of rib and spar placement. This results in the outer mould line parametrisation of the semi-wing shown in Figure 2 [17]. A short description of each parameter is shown in Table 1 [17]. The parametrisation is devised from an inside-out approach to accommodate the passenger cabin and payload bay, depicted by the dashed lines, in a volume-efficient way. This means that the inboard wing, ending at section 3, is fully dictated by the shape of the cabin. As mentioned in Section I, the focus of the aerodynamic shape optimisation is therefore placed on the outer wing which extends from section 3 up to section 5. The inside-out approach also leads to a different parametrisation for the inboard and outboard wing sections. While sections 1, 2 and 3 are determined by the oval cabin at that location, sections 4 and 5 are described using CST coefficients. The CST coefficients method developed by Kulfan [18] represents an efficient way to describe an airfoil section with a minimum amount of design variables while still ensuring design flexibility.
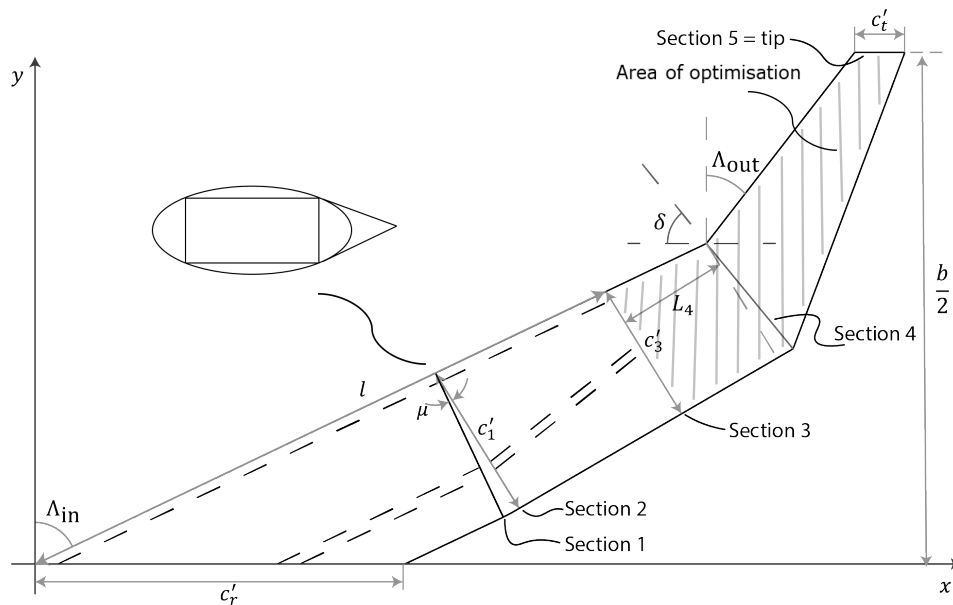
Fig. 2   Semi-wing planform parametrisation by Hillen [17].

The complete geometry is built from linear lofted surfaces between each section, these so-called trunks extend from one section to the next. The wing trunk constructed using sections 1 and 2 is a special case; sections 1 and 2 can possess the same leading edge point while their trailing edge points are positioned based on the angle μ. This results in a trunk in which the major and minor radius are the same, i.e., a horn torus [17]. The toroidal geometry causes a change in the trailing edge sweep angle such that the trunk lofted between sections 2 and 3 is tapered. Another point of attention is the trunk located between sections 3 and 4. As the sections are parameterised differently, the linear lofted trunk connects

---

[¶]Salome Mesh, Retrieved on 29-04-2022 from `https://docs.salome-platform.org/7/gui/SMESH/index.html`
[‖]Stanford University Unstructured (SU2), Retrieved on 29-04-2022 from `https://su2code.github.io/`

Table 1   Wing planform parameters [17].

Symbol	Parameter	Unit
b	Span	m
$\overline{c}_1'$	Normalised chord length of section 1	-
Λ_{in}	Inboard leading edge sweep angle	°
Λ_{out}	Outboard leading edge sweep angle	°
λ	Overall taper ratio $\frac{c_r}{c_t}$	-
$\overline{L}_4$	Normalised length positioning the leading edge kink	-
$\overline{c}_3'$	Normalised chord length of section 3	
δ	Orientation angle of section 4	°
μ	Torus section angle	°

two cross-sectional geometries which are inherently different. This results in a radical cross-sectional shape change over a short spanwise distance. Additionally, as the sweep angle of the outboard wing is significantly lower than the inboard sweep angle, sharp leading and trailing edge kinks are present.

From an aerodynamic analysis point of view, the mentioned geometric characteristics are not desired. The toroidal section is difficult to mesh as the leading edge of the section is a singular point. Furthermore, the sharp changes in the leading and trailing edge sweep angles can cause undesirable aerodynamic effects. However, the most critical point of the geometry is located at the linear lofted trunk between sections 3 and 4. As the change in cross-sectional shape is located at an angle with respect to the free stream direction, the cross-sectional shape in this direction exhibits C0 discontinuities. As Hillen demonstrated, these discontinuities lead to strong shock waves over the outboard wing degrading the aerodynamic performance of the entire Flying V [17]. The goal of the geometric model developed for this study is to remove the undesired aerodynamic characteristics of the parametrisation, while still maintaining its structural efficiency.

The solution is found in a new way to loft the trunks: instead of using linear lofted surfaces, Gordon surfaces are used. Gordon surfaces are constructed using closed networks of curves in the parametric $u - v$ space. In this parametric space, there must be intersection points where the curves cross each other's plane, and no curves should end in a single point, i.e., all curves should end in an intersection point. An example of a closed network of curves is shown in Figure 3. The curves in the $u - v$ space can also be seen as guides and profiles, where guides are indicated by $f_i(u)$, and profiles by $g_j(v)$, with i and j being the index of the respective guides and profiles. The resulting Gordon surface is generated following a curve network interpolation method developed by W.J. Gordon [19, 20]. Four main steps can be distinguished, which are visualised in Figure 5:

1) A skinning surface ** $S_u(u, v)$ is created by interpolating the curves $f_i(u)$, $\forall i$.
2) A skinning surface $S_v(u, v)$ is created by interpolating the curves $g_j(v)$, $\forall j$.
3) A surface $T(u, v)$ is created by interpolating the intersection points of the curve network.
4) The Gordon surface is constructed following a superposition of these surfaces according to:

$$G(u, v) = S_u(u, v) + S_v(u, v) - T(u, v) \tag{1}$$

In the case of a wing, the guides represent the leading and trailing edges, and the profiles represent the airfoil's upper and/or lower curves. To generate the guides in the case of the Flying V, the initial linear lofted geometry is used as a basis. The leading and trailing edge of the linear lofted trunks is sampled in the spanwise direction, resulting in two sets of points. These points serve as control points for B-splines describing the leading and trailing edges. The use of B-splines provides more control over the leading and trailing edge kinks present at the torus section and in the outboard wing. This is due to the mathematics behind B-splines. Consider Figure 4 [20] and Equation 2, where $\overline{P_i^c}$ represent the control points vector, $N_i^d(u, \overline{t})$ the B-spline basis functions, and $\overline{t}$ the knot vector. The higher the number of knots, i.e., the degree of the resulting B-spline $c(u)$, the closer the B-spline is to pass through each control point. Thus, in the case of the Flying V, adjusting the degree of the B-spline provides control over the sharpness of the kinks in the leading and trailing edges.

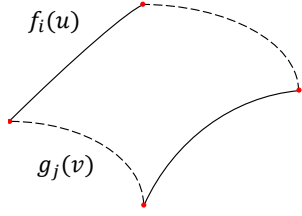**A skinning surface is a non-unique surface containing a set of curves.
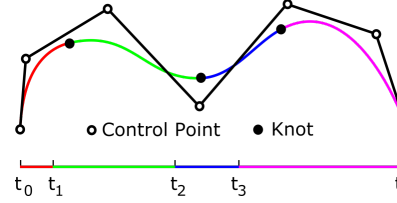
Fig. 3   A closed network of curves.

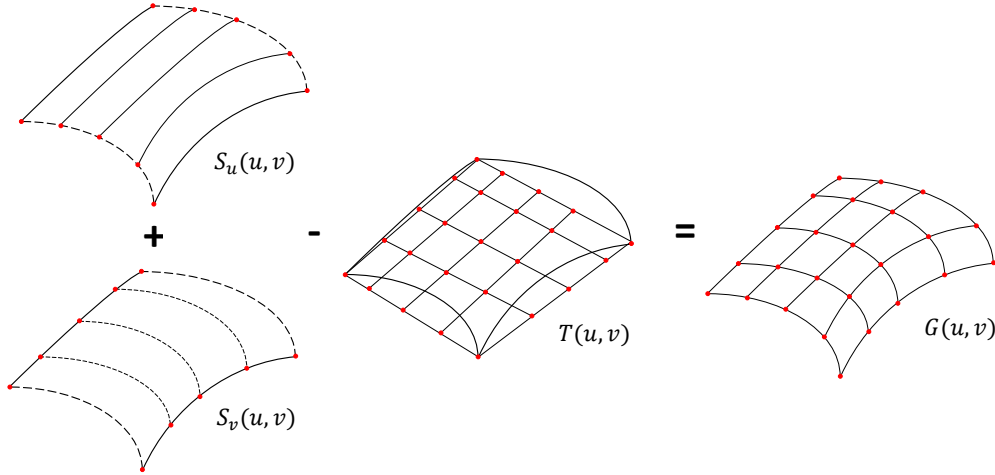**Fig. 4   B-spline approximation [20].**

Fig. 5   Build-up of a Gordon surface according to the superposition principle.

$$c(u) = \sum_{i=0}^{n} \overline{P_i^c} \cdot N_i^d(u, \bar{t}) \tag{2}$$

The new lofting technique is implemented for sections 1 up to 5. Leaving the first part of the inboard wing as a linear lofted trunk as it has a constant cross-section along its length. While this study is solely focused on re-designing the outboard wing, the trunks between sections 1 and 3 are adjusted as well to remove the undesired torus section. The outline used for generating the Gordon surfaces is shown in Figure 6, including both the leading and trailing edge guides, and the airfoil's profiles. Note that by applying the Gordon surfaces lofting technique, sections 2 and 4 become redundant. This means that the variables needed to describe both sections can be removed from the parametrisation without reducing the design flexibility. The angle δ is however still relevant as this in essence determines the position of the trailing edge kink with respect to the leading edge kink.

The complete geometry used in the subsequent aerodynamic design process is shown in Figure 7. Note that for completeness of the aerodynamic analysis, the cockpit, centre body fairing, and winglets are included in the geometry as well. These components have a significant effect on the aerodynamic performance and therefore must be considered to provide definitive proof for the research objective. The cockpit and centre body fairing design were devised by Brouwer [14], while the winglets were designed by Horwitz [15]. The initial geometry of the wing is based on the design variables found by Oosterom, who conducted a study into the family design of the Flying V [16]. The current study uses the design variables related to the largest Flying V version of the family, the FV-1000, as it is the most aerodynamically critical design due to its large wetted area. Moreover, all Flying V versions in the family possess the same outboard wing, hence optimising the wing for the largest version also suffices for the smaller aircraft.

An additional module is developed to generate the design of the outboard wing control surfaces or elevons. The control surface integration can impact the design flexibility of the outboard wing. Hence, neglecting them in the shape optimisation process can result in unfeasible designs when trying to implement the control surfaces afterwards. The design of the control surface is mainly based on the positioning of the hinge line. For an effective deflection of the

6
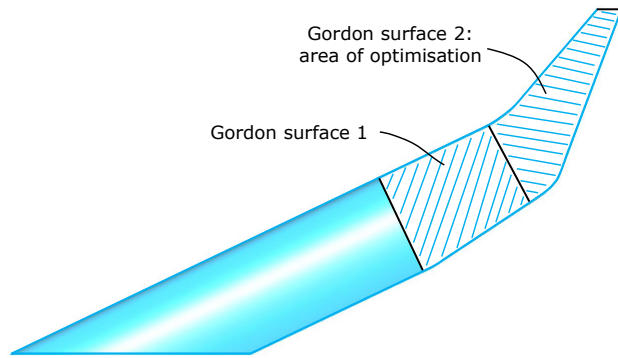
Fig. 6   Curve network of the semi-wing planform.
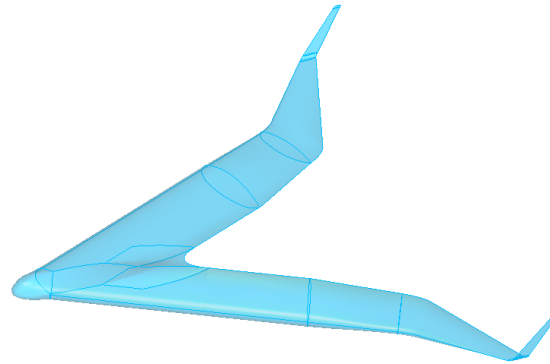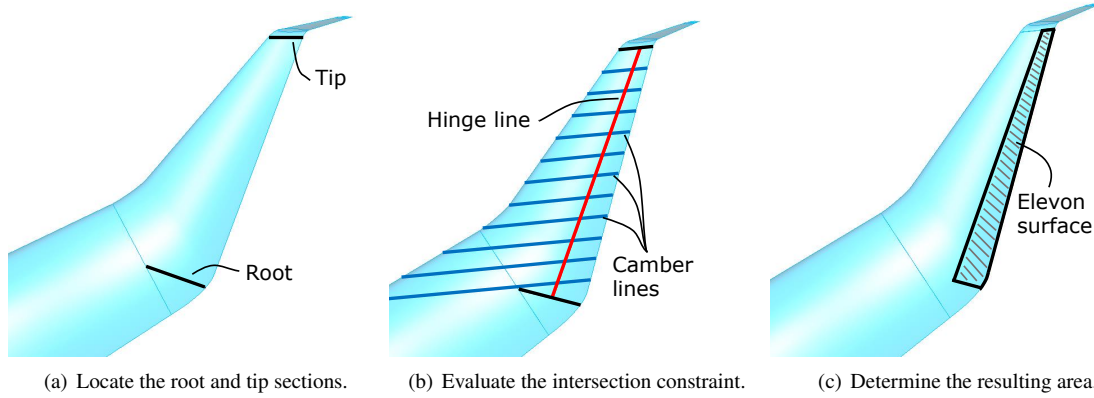

Fig. 7   Complete Flying V geometry.

surface, the hinge line must be straight and pass through the camber lines of all intermediate airfoil sections. This immediately poses a strict constraint on possible hinge line locations. Also, the root and tip sections of the control surface must be positioned. Based on the Flying V sub-scale flight test model [21], it is decided to place the root of the control surface perpendicular to the trailing edge of the outboard wing, while the tip is defined as section 5 of the planform parametrisation. It must be noted that the most forward x/c location of the hinge line at the tip (section 5) is limited to result in a control surface with a maximum chord length of $35\%\,c$. This value is based on the fact that the effectiveness of the control surface does not increase to a greater extent when the chordwise dimension is further increased [22]. Moreover, the torque box supporting the winglets needs to be positioned in front of the control surface and requires appropriate space as well. The main steps of the control surface generation process are explained below, and visualised in Figure 8:

1) The root and tip sections of the control surface are generated, and points along their camber lines are sampled. These represent the starting and end points of possible hinge line locations respectively.
2) Feasible hinge line locations are determined according to a constraint satisfaction problem, which states: to find a combination of starting and end points between which a straight hinge line can be formed satisfying the camber line intersection constraint. This problem is broken down as follows:

    a) For each combination of starting and end points, a straight line is drawn between them to generate a hinge line.
    b) For each hinge line location, the camber lines of the airfoil sections through which the hinge line passes are obtained.
    c) For each airfoil section, the offset δs between the hinge line and the camber line is determined in the airfoil's plane.
    d) For each hinge line location, the maximum offset between the hinge line and the camber lines is determined.
    e) For each maximum offset, the value is compared to a predetermined maximum allowed offset. If the maximum offset of a hinge line location is smaller than this value, it is considered a valid location.

3) The best location of all valid hinge line locations is qualified by the largest resulting surface area for the control surface.

B. Aerodynamic Design Strategy

As stated in Section I, the main goal of this study is to obtain the maximal lift-to-drag ratio of the Flying V by re-designing the outboard wing through a constrained aerodynamic shape optimisation. This process is divided into multiple steps which are visualised in Figure 9. The process starts with converting the linear lofted geometry (*linear design (0)*) into the Gordon surfaces lofted wing (*initial design (1)*) using the geometric model as explained in Section II.A. Subsequently, a low-fidelity optimisation process of the planform parameters is conducted to develop *baseline design (2)*. This baseline design serves as input to the higher-fidelity Free-Form Deformation (FFD) shape optimisation. Two different approaches are considered for this final optimisation step depending on the integration of the outboard control surfaces. When integrating these surfaces into the wing design, the FFD optimisation consists of two steps, whereas neglecting the

7

(a) Locate the root and tip sections.   (b) Evaluate the intersection constraint.   (c) Determine the resulting area.

Fig. 8   Automated control surface sizing sequence (top view).

integration only requires one optimisation step. The latter results in the *single step design (3)*, while the former leads to the *dual step design (4)*. The baseline and FFD optimisation steps are explained in the subsequent sections.
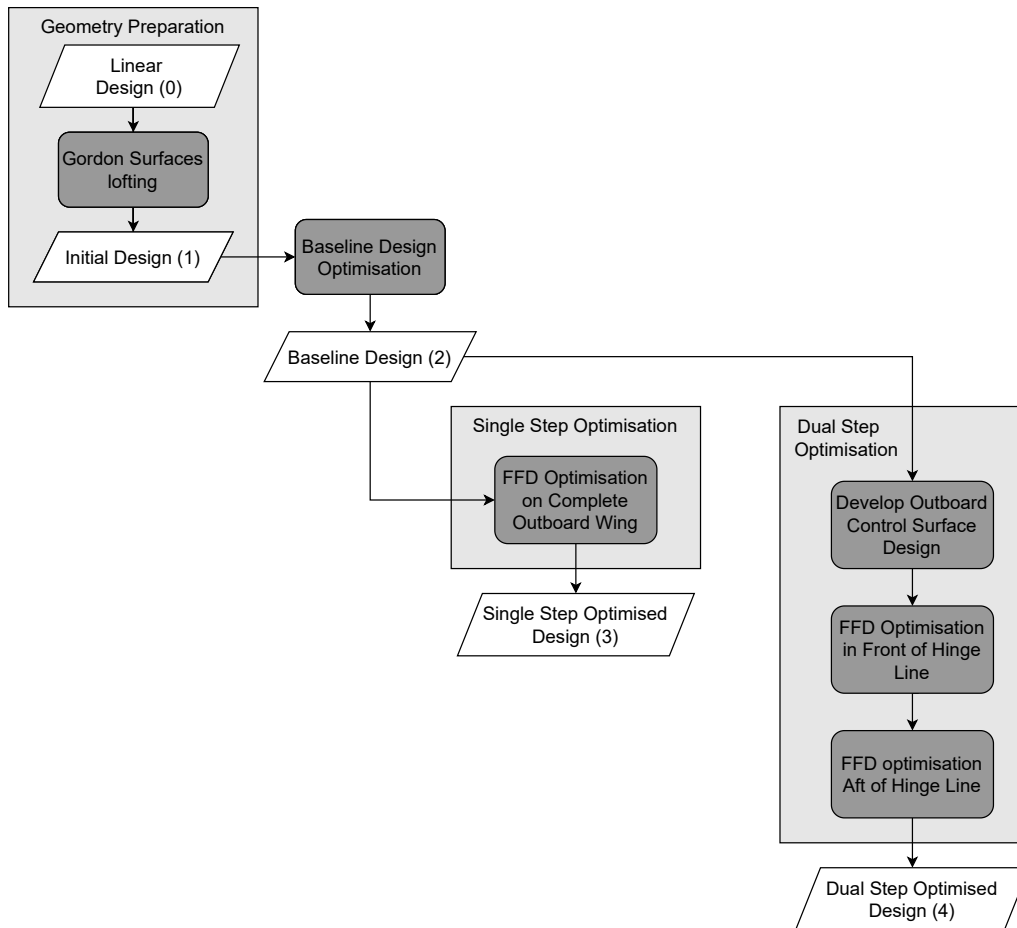
1. Baseline Design Optimisation

The baseline design optimisation is performed to efficiently move towards a starting point for the FFD aerodynamic shape optimisation. The baseline optimisation adjusts planform parameters and incorporates several predetermined design changes, while the FFD optimisation tailors the cross-sectional shape of the wing. The baseline optimisation procedure consists of two main steps which are visualised in Figure 10. First, an automated low-fidelity optimisation process is conducted, whereafter the resulting optimised design is evaluated using a higher-fidelity flow model and the control surface sizing module. The objective of the automated optimisation process is to adjust the planform parameters such that an elliptical lift distribution is obtained. This optimisation is coordinated by the Differential Evolution (DE) algorithm, a type of genetic algorithm developed by Storn and Price [23]. It is a gradient-free algorithm which can find the global optimum of nonlinear and non-differentiable objective functions in a robust way. Furthermore, its favourable convergence behaviour in combination with its parallel computing capabilities make it suitable for this type of application. In mathematical terms, the optimisation can be expressed as follows:

$$\begin{aligned}
\min \quad & \Delta E(\bar{x}) \\
\text{s.t.} \quad & -2.5 \leq \Delta S_{\text{ref}} \leq 2.5 \\
& b \leq 32.5
\end{aligned} \tag{3}$$

The objective is formulated such that the difference between the actual lift distribution and a perfectly elliptical distribution is minimised. The design variables used in the optimisation are the taper ratio λ, the half span of the wing b, the location of the leading edge kink L_4, the outboard sweep angle Λ_{out}, the orientation of section 4 δ (or the location of the trailing edge kink with respect to the leading edge kink), and the tip section incidence angle ϵ_5. The latter is added to the planform variables as airfoil incidence angles are effective in adjusting the resulting lift distribution. This lift distribution is obtained by analysing the designs using Athena Vortex Lattice (AVL), a linear vortex lattice method (VLM) capable of efficiently outputting aerodynamic force coefficients [24]. The optimisation is also subjected to inequality constraints stating that the change in the aircraft's reference area cannot be larger than 2.5 m² and that the span of the semi-wing cannot exceed 32.5 m. The first originates from the idea of maintaining the same wing loading considering low-speed requirements, while the latter is dictated by span constraints at airports.

The resulting optimised design is subsequently analysed using the higher-fidelity Euler equations model of the Stanford University Unstructured (SU2) solver to validate the results of the optimiser [25]. Additionally, the control surface is sized to test the feasibility of the wing design. These results are used in the comparison of the optimised design against the *initial design (1)*. The designs are compared according to several criteria, including the strength of the shock wave (if present), the maximum local Mach number, the size of the control surface as derived from the sub-scale flight test model [26], and the size of the tip airfoil considering structural constraints. When the optimised design is deemed insufficient, changes to the DE algorithm set-up are made to induce the generation of new designs.

8

Fig. 9   Aerodynamic design strategy of the Flying V outboard wing.

This process is repeated until a satisfactory optimised design is found, leading to *baseline design (2)*.

Several design changes are incorporated into the generation of the *baseline design (2)*. Earlier studies regarding the structural design of the Flying V noted that the tip airfoil size is insufficient to efficiently carry the loads generated by the winglets [27]. This tip airfoil is described by the overall taper ratio and CST coefficients found in the family design study by Oosterom [16]. This study resulted in an overall taper ratio of 0.1, and a tip airfoil having a thickness-to-chord ratio of 9.6%. While this low taper ratio and small thickness are desired from an aerodynamic perspective, it results in a heavy tip structure to be able to support the loads of the winglets. To improve the structural feasibility of the outboard wing design, it is decided to incorporate these findings by placing a lower bound on the taper ratio of 0.12 and including a transonic tip airfoil having an 11% thickness-to-chord ratio in the free stream direction. The criterion for assessing the optimised designs, therefore, requires that the tip airfoil has a thickness-to-chord ratio of more than 11% and a taper ratio of more than 0.12. These changes cause an increase of 37.5% in the thickness of the tip airfoil, resulting in a 90% increase in the second moment of area and thus a lighter tip structure. This means that the resulting outboard wing design is not only feasible from an aerodynamic perspective but is also structurally sound.

2. Free-Form Deformation Shape Optimisation

After the planform is optimised in the baseline design process, the cross-sectional shape of the wing is altered through an FFD aerodynamic shape optimisation using SU2. The main steps of the SU2-based shape optimisation are visualised in Figure 11. The inputs to the design process are the FFD parameterised geometry in the form of a computational mesh, the chosen objective function $f(\overline{x})$ and constraints $g_i(\overline{x})$, and the vector containing the design variables $\overline{x}$. After the performance of the design is evaluated using the flow analysis, the gradients of the objective $\nabla f(\overline{x})$ and constraints

9
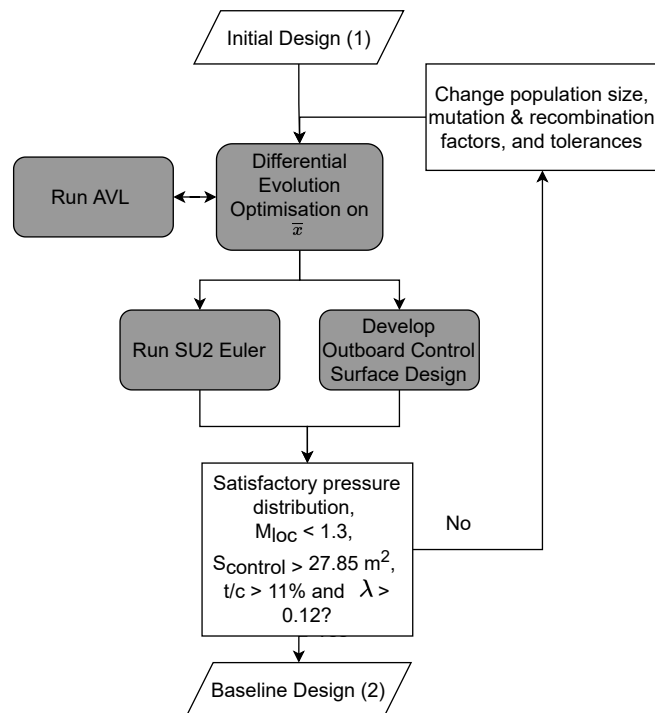
Fig. 10   Multi-fidelity baseline design optimisation strategy.

$\nabla g_i(\overline{x})$ are obtained using a continuous adjoint method. This initiates a gradient-based optimisation algorithm which guides the design cycle towards an optimum $\overline{x}*$. The algorithm used is the Sequential Least Squares Programming (SLSQP) optimiser, which terminates the design loop if the Karush-Kuhn-Tucker (KKT) conditions are met, or if the maximum number of iterations (100) is reached [28].

The FFD parametrisation approach is an efficient way to describe a geometry and its deformation. It parameterises the deformation of the geometry rather than the geometry itself [9]. This is done by placing a so-called FFD box around the geometry that is to be deformed. The sides of the box contain control points which represent the design variables in $\overline{x}$. This box is visualised in Figure 12. The control points are defined in the parametric space while the geometry itself is described in the physical space by surface mesh nodes. To link the control points with the physical coordinates of the geometry, a mapping using a trivariate tensor product Bernstein polynomial is performed. The use of Bernstein polynomials provides the ability of local deformations while ensuring continuity of the geometry [29]. A deformation using FFD can be described by three main steps [30]:

1) The geometry described in the physical space is mapped to the parametric space of the FFD box. During this mapping, the parametric coordinates of every point in the physical space are determined. This mapping only has to be performed once.
2) A perturbation is imposed on the FFD box control points leading to the deformation of the box as well as the geometry in the parametric space.
3) The new coordinates of the geometry in the physical space are determined using Bernstein polynomials and the developed mapping between the parametric and physical space.

Note that the mesh serving as input to the shape optimisation process must already contain information on the mapping of the geometry onto the parametric space. As this mapping is only required once, it is not part of the design loop. After the surface mesh of the geometry is deformed in both the parametric and physical space, the volume mesh surrounding the object is deformed as well. The technique implemented in SU2 makes use of the equations of linear elasticity to model the volume mesh as an elastic solid [31]. The quality of the deformation can be controlled by the modulus of elasticity for each volume mesh cell. In particular, this modulus must be inversely proportional to the cell

10
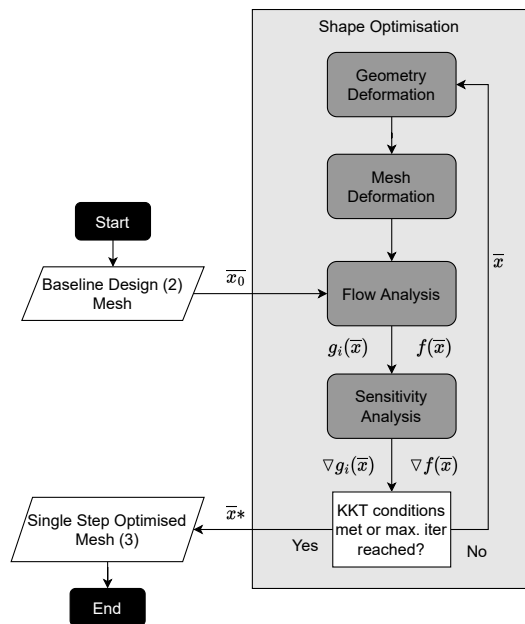
Fig. 11 FFD gradient-based shape optimisation of SU2.

volume to preserve the mesh quality [30]. The use of the mesh deformation module eliminates the need to re-mesh every design iteration, reducing the computational time. While the elastic solid approach is robust for inviscid meshes, it is unstable for meshes including prism layers which are used in Reynolds-Averaged Navier-Stokes (RANS) flow analyses to capture the viscous boundary layer effects. Consequently, the FFD shape optimisation is performed using the inviscid Euler equations to ensure a constant mesh quality throughout the entire optimisation process. Moreover, the Euler equations are computationally less demanding.

The objective of the FFD aerodynamic shape optimisation is to reduce the drag coefficient of the design while satisfying several constraints. First, an equality constraint on the lift coefficient is imposed such that $C_L = 0.26$. This value is determined by analysing the drag polar for the FV-1000 as obtained by Oosterom [16]. In the second place, the pitching moment coefficient around the centre of gravity must be within the bounds of $-0.01 \leq C_m \leq 0.01$ to minimise the trim drag of the aircraft [32, 33]. Trim drag in blended-wing-body aircraft is critical as the distance of the control surfaces to the centre of gravity is less compared to conventional aircraft, resulting in larger required deflections. The centre of gravity of the Flying V is located at 52.8% of the total aircraft length as measured from the aircraft's nose when the cockpit is not integrated [34–36]. After the integration of the cockpit, the nose is blunter resulting in the $x=0$ location (x is in the direction along the aircraft's length) to be located ahead of the aircraft's actual nose. Moreover, to maintain a structurally feasible wing design, the thickness-to-chord ratio of the outboard wing sections is required to be larger than 11%. This is similar to the tip airfoil constraint imposed in the baseline design optimisation. In mathematical terms, the optimisation can be expressed as follows:

$$
\begin{aligned}
\min \quad & C_D(\overline{x}) \\
\text{s.t.} \quad & -0.010 \leq C_m \leq 0.010 \\
& t/c_i \geq 0.11 \\
& C_L = 0.26
\end{aligned}
\tag{4}
$$

A continuity constraint is imposed on the geometry to ensure a G2 continuity level at the intersection of the FFD box and the existing aircraft geometry. This is implemented by adjusting the design variables, i.e., control points of the FFD box, in $\overline{x}$. By imposing the continuity constraint, control points near the planes where this constraint is active are not allowed to move and can thus be removed from the design vector. The planes on which this constraint is active are the root (section 3) and the tip (section 5) of the outboard wing. The root section of the wing is namely dictated by the cross-sectional shape of the cabin and is therefore not allowed to change. The cross-sectional shape of the tip is fixed due to compliance requirements with the geometry of the adjacent winglet. These planes also correspond to the root and

11

tip planes of the FFD box shown in Figure 12.

Finally, the integration of the outboard control surfaces is considered as well. This integration introduces an additional constraint which is incorporated via the FFD box setup. The requirement for a feasible control surface is that its hinge line must pass through the camber lines of all intermediate airfoil sections. A control surface satisfying this requirement is established for *baseline design (2)*. However, when optimising the shape of the wing using the FFD approach, forming a control surface afterwards might not be possible anymore as the camber lines of the wing sections can change significantly. This problem is solved by fixing the control points in the plane of the hinge line of *baseline design (2)* during the optimisation. Consequently, the FFD optimisation consists of two steps: first the wing shape in front of the hinge line is optimised after which the geometry aft of the hinge line is optimised. This approach requires the use of two different FFD boxes which are positioned based on the location of the hinge line, see Figures 13 and 14. Imposing a continuity constraint on the hinge line plane in the FFD boxes results in a fixed geometry, and thus camber lines, in that plane. This means that the baseline control surface design is still valid for the optimised wing. This two-step approach is visualised in Figure 9, and results in the *dual step design (4)*. Also, an FFD optimisation without considering the control surface integration is conducted to evaluate the effect of this constraint. This optimisation is performed in one step using the FFD box visualised in Figure 12, resulting in the *single step design (3)*.
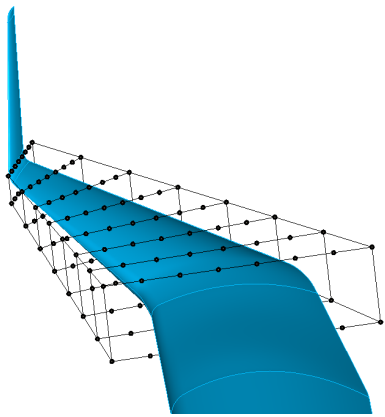
Fig. 12   FFD box around the complete outboard wing of the Flying V.
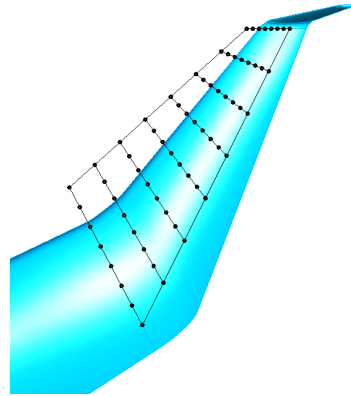
Fig. 13   FFD box in front of the hinge line (top view).
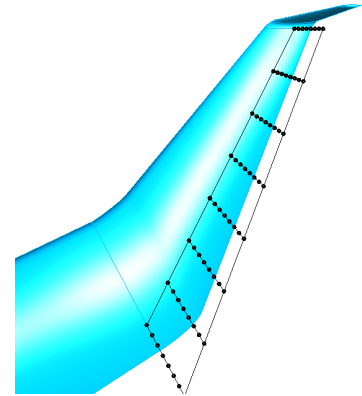
Fig. 14   FFD box aft of the hinge line (top view).

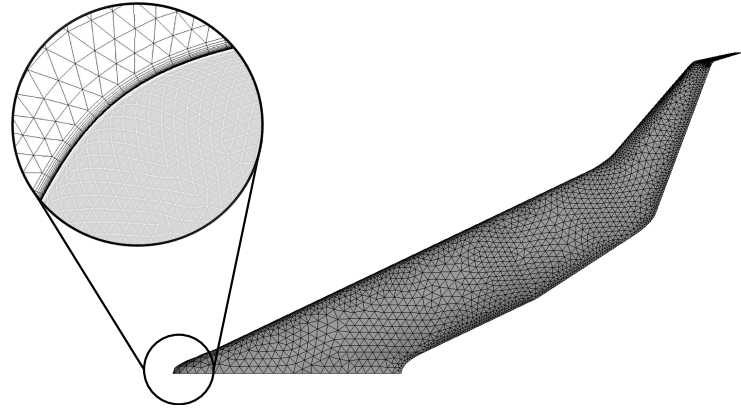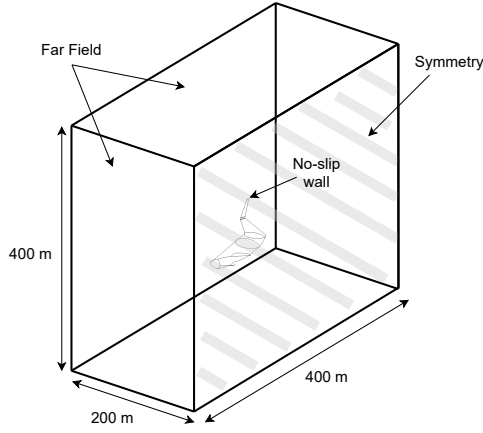## C. Flow and Sensitivity Analysis Modules

Various aerodynamic flow models are used in the aerodynamic shape optimisation process as discussed in Section II.B. The baseline design optimisation relies on the linear VLM method of AVL and the Euler equations model of SU2, while the FFD shape optimisation solely relies on the Euler equations of SU2. As the Euler equations assume an inviscid flow, the flow results of the FFD shape optimisation (for *single and dual step designs (3, 4)*) are augmented with the empirical viscous drag module developed by Faggiano [12]. Furthermore, to provide a better insight into the contributions of the pressure and friction drag components, *linear design (0)*, *initial design (1)*, and *baseline design (2)* are analysed using the RANS flow model of SU2 which does capture viscous boundary layer effects. To be able to compare the aerodynamic performance of all designs, also *baseline design (2)* is analysed using the Euler flow model augmented with the viscous drag module to correlate the performance of the module with the RANS equations.

The viscous drag module of Faggiano [12] estimates the profile drag of the aircraft, which can be divided into skin friction, pressure, and lift-induced profile drag. An estimation for the latter drag component is not included in the module as this can safely be omitted when performing the analysis in cruise condition [12, 37]. The other components are estimated according to Equation 5, where C_f is the skin friction coefficient in the free stream direction, f the form factor of each aircraft component, S_{wet} the wetted area, and S_{ref} the reference area of the wing. The form factor represents the pressure drag due to viscous flow separation on the wing and winglets. Its value is computed using semi-empirical relations proposed by Raymer [38]. The augmented lift-to-drag ratio is subsequently computed via Equation 6, where $C_{D\text{inv}}$ represents the inviscid drag coefficient obtained by the Euler equations. The flow model consisting of the SU2 Euler flow solver augmented with the viscous drag module is hereafter called the Euler+ model.

$$C_{D_0} = C_f \cdot f \cdot \frac{S_{\text{wet}}}{S_{\text{ref}}} \qquad (5) \qquad\qquad \frac{C_L}{C_D} = \frac{C_L}{C_{D_0} + C_{D\text{inv}}} \qquad (6)$$

Using the implemented APIs in ParaPy for both Salome Mesh and SU2, an unstructured mesh for the computational domain, and the required configuration file for SU2 are generated. The configuration file contains information on the numerical solver settings, flight and boundary conditions, convergence criteria, and reference values. The computational domain used for the CFD analyses is shown in Figure 15. A half model is used in the flow analysis by imposing a symmetry condition at the symmetry plane of the domain. The free stream conditions are modelled by imposing the far field boundary condition incorporated in SU2. The far-field boundary of the domain is located at a distance of 20 body lengths from the aircraft, as suggested by Chan et al. [39]. When using the inviscid Euler equations to describe the flow, an Euler wall boundary condition is imposed on the surface of the aircraft. While in the case of the viscous RANS equations, an adiabatic no-slip wall condition is imposed instead to capture the zero advection velocity near the surface. Additionally, a refined mesh in the regions where these viscous effects are prevalent is required. Compared to the unstructured Euler mesh used in the baseline design process and the FFD shape optimisation, additional prism layers are incorporated near the aircraft's surface to fully resolve the boundary layer. An example of a coarse mesh with prism layers generated using Salome Mesh is shown in Figure 16.

Fig. 15 Computational domain including dimensions and boundary conditions.

Fig. 16 Example of a coarse mesh including prism layers for a half model of the Flying V.

Next to the flow analysis, the FFD optimisation requires a sensitivity analysis as well to generate the gradients for the optimiser. The gradient for the objective function as well as for the constraint functions are obtained via [25]:

$$
\begin{bmatrix}
\frac{\partial f}{\partial x_1} \\
\frac{\partial f}{\partial x_2} \\
\vdots \\
\frac{\partial f}{\partial x_n}
\end{bmatrix}
=
\begin{bmatrix}
\frac{\partial s_1}{\partial x_1} & \cdots & \frac{\partial s_m}{\partial x_1} \\
\vdots & \ddots & \vdots \\
\frac{\partial s_1}{\partial x_n} & \cdots & \frac{\partial s_m}{\partial x_n}
\end{bmatrix}
\cdot
\begin{bmatrix}
\frac{\partial f}{\partial s_1} \\
\frac{\partial f}{\partial s_2} \\
\vdots \\
\frac{\partial f}{\partial s_m}
\end{bmatrix}
\qquad (7)
$$

Where n represents the number of control points; m the number of surface mesh nodes in the physical space; f the function for which the gradient is sought; x_i are the design variables (i.e. control points) with $i = 1, 2, ..., n$; and s_j represent the surface normal displacements of mesh nodes $j = 1, 2, ..., m$. The gradients of every design variable $\delta f/\delta x_i$ can be obtained via the dot product between the geometric sensitivities $\delta s_m/\delta x_n$ and the surface sensitivities $\delta f/\delta s_m$. The surface sensitivities represent the change in f due to a small change in the local surface normal, i.e., a change in the geometry. These surface sensitivities are computed at every mesh node m by solving a continuous adjoint equation. The geometric sensitivities indicate the change in the control points due to a change in the surface mesh nodes and are obtained using a finite difference approach. The computational effort of solving the adjoint equation is equal to obtaining one flow solution, while the computational effort to obtain the geometric sensitivities is negligible as it is not based on any flow solution. This results in a gradient evaluation which is virtually independent of the number of design variables which is beneficial for gradient-based optimisers such as the SLSQP algorithm. Furthermore, in combination with the FFD box control points, the high number of possible design variables is advantageous for the design flexibility.

13

III. Verification & Validation

To determine the validity of the models and computational grid used for this research, several verification and validation steps are performed. This section discusses the mesh convergence and mesh quality studies, after which the aerodynamic solver validation is presented.

A. Mesh Convergence Study

To determine the number of cells needed to effectively capture the aerodynamic phenomena, a grid convergence study is performed. The goal of the study is to determine the size of the coarsest mesh yielding acceptable results. More specifically, during an aerodynamic optimisation process, the exact values of the aerodynamic coefficients are less important than resolving the governing aerodynamic effects. The mesh refinement has a larger influence on the resulting aerodynamic coefficients of the viscous RANS equations as opposed to the inviscid Euler equations as the boundary layer needs to be resolved. Consequently, the mesh convergence study is conducted using the RANS model of SU2. The various meshes including prism layers are generated using Salome Mesh. The results of the mesh convergence study are shown in Figure 17 and Table 2. Note that the relative error is determined with respect to the finest grid of over 8 million cells. As the flow model is based on the RANS equations, both the pressure and friction drag components are resolved. As seen in Table 2, the coarsest meshes overestimate the contribution of the pressure drag to the complete drag coefficient, meaning that the viscous effects in the boundary layer are not sufficiently resolved. Consequently, it is determined that the mesh with around 6 million cells would provide sufficiently accurate results for the aerodynamic shape design process. This is further supported by the relative error of 0.3% and 2.1% for the drag coefficient and pitching moment coefficient respectively. The resulting mesh size is also deemed valid for Euler analyses as the results are less sensitive to the mesh refinement due to their inviscid nature.

(a) Aerodynamic coefficients convergence.

(b) Relative error w.r.t. the finest grid.
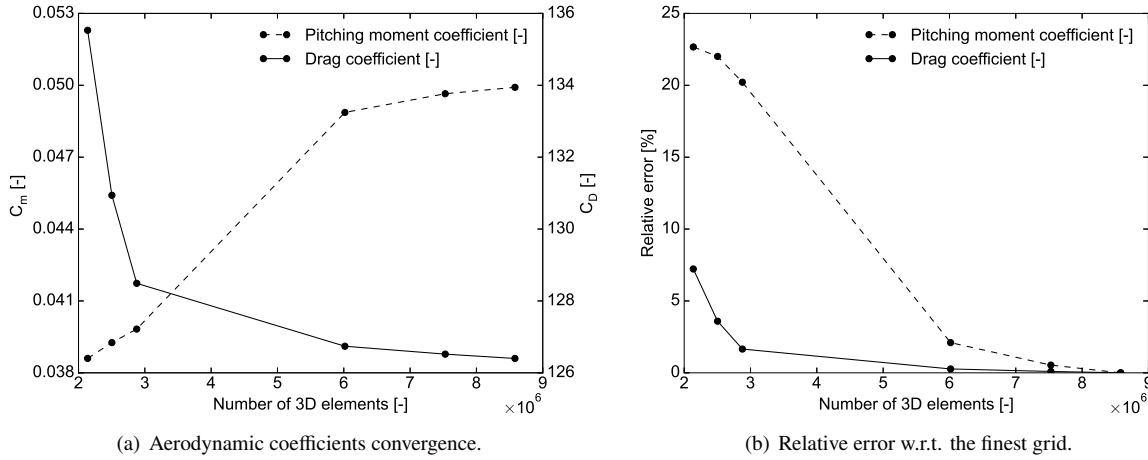
Fig. 17   Salome Mesh grid convergence study at $M = 0.85$ and $C_L = 0.26$.

Table 2   Salome Mesh grid convergence study of the drag coefficient components.

Number of 3D elements	C_D [-]	C_{D_p} [%]	C_{D_f} [%]
2.14×10^6	135.53	60.64	39.36
2.50×10^6	130.94	59.36	40.64
2.88×10^6	128.49	58.76	41.24
6.16×10^6	126.74	57.66	42.34
7.53×10^6	126.52	57.84	42.22
8.58×10^6	126.40	57.81	42.19

14

B. Mesh Quality Study

After the approximate size of the required mesh is determined, the quality of the mesh is evaluated. This is done by analysing the quality metrics related to (viscous) meshes. The most important metric for meshes with prism layers is the non-dimensional first layer height y^+. This value should be equal to, or less than, one to effectively capture the boundary layer effects [39]. If the value is higher than one, the nodes of the first prism layer lay outside the boundary layer meaning that its velocity gradient cannot be captured. The y^+ value is obtained from the flow solution of SU2. Its resulting distribution is shown in Figure 18. Note that the histogram is focused on the range of y^+ values between 0 and 0.25 as the number of cells with a y^+ value between 0.25 and 1 is too small to be visualised. Nevertheless, several cells near the trailing edge of the winglet tip exhibited a y^+ value near 0.8 which is shown in Figure 18b. This can be ascribed to the constant first layer height over the entire aircraft surface in combination with the local boundary layer thickness.

(a) First layer height distribution.

(b) First layer height distribution on the winglet.
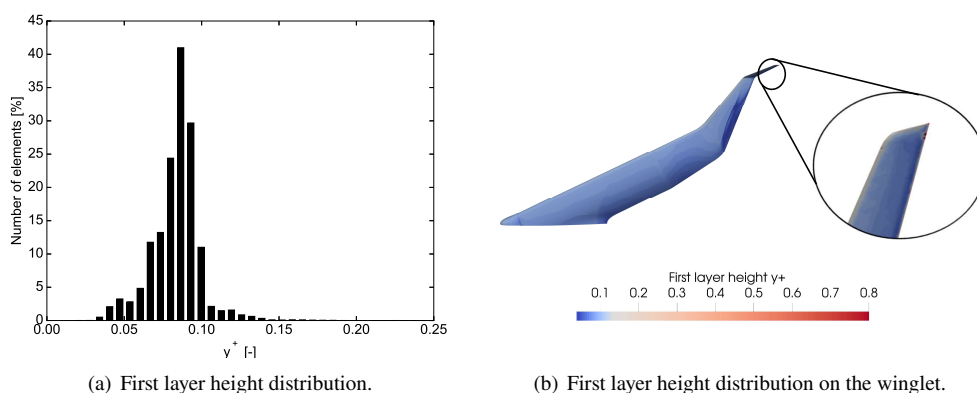
Fig. 18   Salome Mesh grid quality study of the first prism layer height.

Additionally, the surface mesh is assessed according to the skew angle and 2D aspect ratio. The skew angle indicates the angular element quality compared to the angles observed in an ideally shaped element, in this case, an equilateral triangle. The skew angle should be as close as possible to 0°; however, the acceptable range is between 0 and 45°[40]. As observed in Figure 19a 66% of the elements have a skew angle lower than 10°, and the highest observed skew angle nears 42°. The latter is deemed acceptable due to its low occurrence rate, and it being lower than the maximum allowed angle. The 2D aspect ratio of the surface elements indicates the level of conformity of an element compared to a non-deformed ideal version of its type, i.e., all edges having the same length. Ideally, the aspect ratio should be near 1, however, a range between 1 and 5 is typically deemed acceptable [41]. As the aspect ratio is based on an equilateral triangle, a value lower than 1 is also possible and deemed acceptable above a value of 0.2. Aspect ratios larger than 5 should be avoided as they can decrease the accuracy of the flow solution. Note that a surface mesh combining elements with an aspect ratio lower and higher than 1 should be avoided as the elements are stretched into different directions resulting in an uneven distribution of the nodes. As observed in Figure 19b, the current grid satisfies the criterion as all observed aspect ratios are between 1 and 2. The Salome Mesh generated grid is therefore deemed satisfactory to use in subsequent analyses.

C. Aerodynamic Model Validation

The SU2 aerodynamic solver described in Section II is validated using experimental data from the Onera M6 wing, which was obtained to serve as a validation model for CFD applications. The Euler version of SU2 was compared to this data by Faggiano and Hillen and is therefore not further discussed [12, 17]. Similarly, the performance of the empirical viscous drag module was verified by Faggiano and Oosterom [12, 16]. Thereupon, this paper focuses on the validity of the RANS model implemented in SU2. Experimental data from test 2308 by Schmitt and Charpin [42] is used to verify the solver in transonic conditions: at a Mach number of 0.8395, an angle of attack of 3.06°and with a Reynolds number of 11.72×10^6. The mesh is obtained from one of the test cases provided by SU2 and consists of 315,806 hexahedral elements. The computational domain is similar to the one visualised in Figure 15. To verify the settings in the configuration file, two different numerical methods to solve the convective flow equations are tested. These include the Jameson Schmidt Turkel (JST) central scheme, which is characterised by stable and fast convergence

15

(a) Skew angle distribution.

(b) 2D aspect ratio distribution.
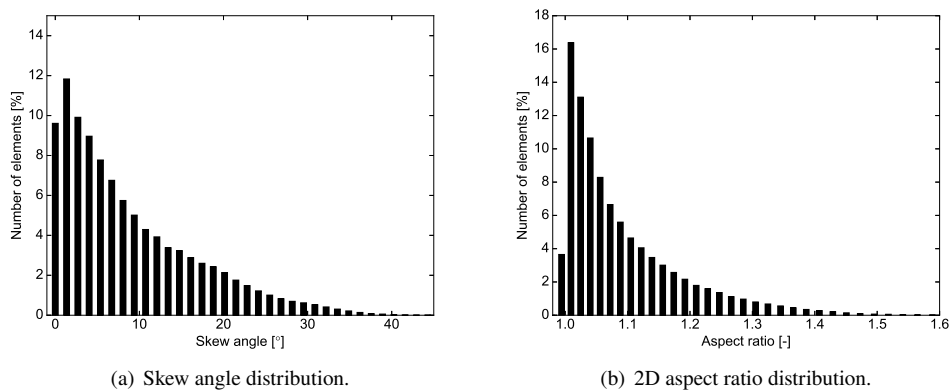
**Fig. 19   Salome Mesh grid quality study of the surface mesh.**

behaviour, and the Roe (ROE) upwind scheme, which is said to be more accurate for a similar mesh refinement [25]. The resulting pressure distributions from the RANS analysis are compared to the experimental data at various spanwise locations of which three are visualised in Figure 20.

Although discrepancies between the numerical and experimental data can be observed, the overall shape of the pressure distributions does bear a resemblance to the experimental data. In Figure 20a, a high suction peak is recorded in the experimental data which is not captured by the numerical simulations. This peak could be attributed to the wall interference of the wind tunnel as this is the most inboard data station. A larger discrepancy is seen in Figure 20b where the strength of the shock waves and the pressure gradients at $x/c = 0.20$ and 0.50 are not captured by the numerical simulations. This discrepancy can be attributed to the limited refinement of the mesh used in the simulations. The ROE convective scheme does however predict the upper surface shock wave better than the JST scheme, supporting the statement that it is more accurate for a similar mesh refinement. Nonetheless, the JST model was deemed sufficiently accurate for the optimisation process as convergence speed is more important than a completely accurate flow prediction.

Additionally, a RANS solver needs a turbulence model to close the system of equations. Several turbulence models are available in SU2 including the Spalart-Allmaras (SA), Spalart-Allmaras with Edwards correction (SA-E), negative Spalart-Allmaras (SA-NEG), and Shear Stress Transport (SST) models [43, 44]. The performance of each is evaluated by comparing it to the experimental data for both the JST and ROE convective models. No significant difference can be observed between the resulting predictions of the simulations for the different turbulence models. Therefore, it is decided to employ the SA model as this was specifically developed for aerospace applications and exhibited beneficial convergence behaviour. This model is also used for the numerical results shown in Figure 20.

As the aerodynamic shape optimisation is driven by the aerodynamic coefficients, it is important to compare these as well. Given that the experimental data of the Onera M6 wing solely contains pressure distributions, the results from the SU2 RANS-SA solver are compared to several numerical studies instead. These studies, conducted by Araya [45], Le Moigne and Qin [46], and Nielsen and Anderson [47], include RANS simulations in combination with various turbulence models. An additional study performed by Crovato et al. [48] is included to also compare the pitching moment coefficient. The results of the SU2 RANS-SA solver and the numerical studies are summarised in Table 3. The relative error between the obtained and the actual lift coefficient is found by integrating the experimentally acquired pressure distributions along the wing. It is observed that the SU2 RANS-SA solver, for both the JST and ROE convective scheme, predicts the lift coefficient within an accuracy of 1.3%, being the second and third most accurate results. The level of agreement indicated by this relative error is also reflected in the pressure drag coefficient. Whereas the SU2 RANS-SA and Araya's RANS-SA and k-ω predictions only vary by a maximum of 2 drag counts, the other studies present a difference of up to 3 to 6 drag counts as compared to the SU2 RANS-SA results. Nonetheless, all results are within 8 drag counts from each other, representing 6% of the average pressure drag.

Slightly more variation is observed in the friction drag component where the maximum difference is 9 drag counts, amounting to roughly 17% of the average friction drag. The larger variation can be attributed to the varying level of boundary layer mesh refinement in the different studies. The SU2 RANS-SA results fall well within the boundaries set by the previously conducted studies, underlining its predictive power. Finally, Crovato et al. also looked at the pitching moment coefficient which is approximately 8% larger than the values found by SU2 RANS-SA. This discrepancy can

16

(a) $\eta = 0.20$

(b) $\eta = 0.65$

(c) $\eta = 0.95$
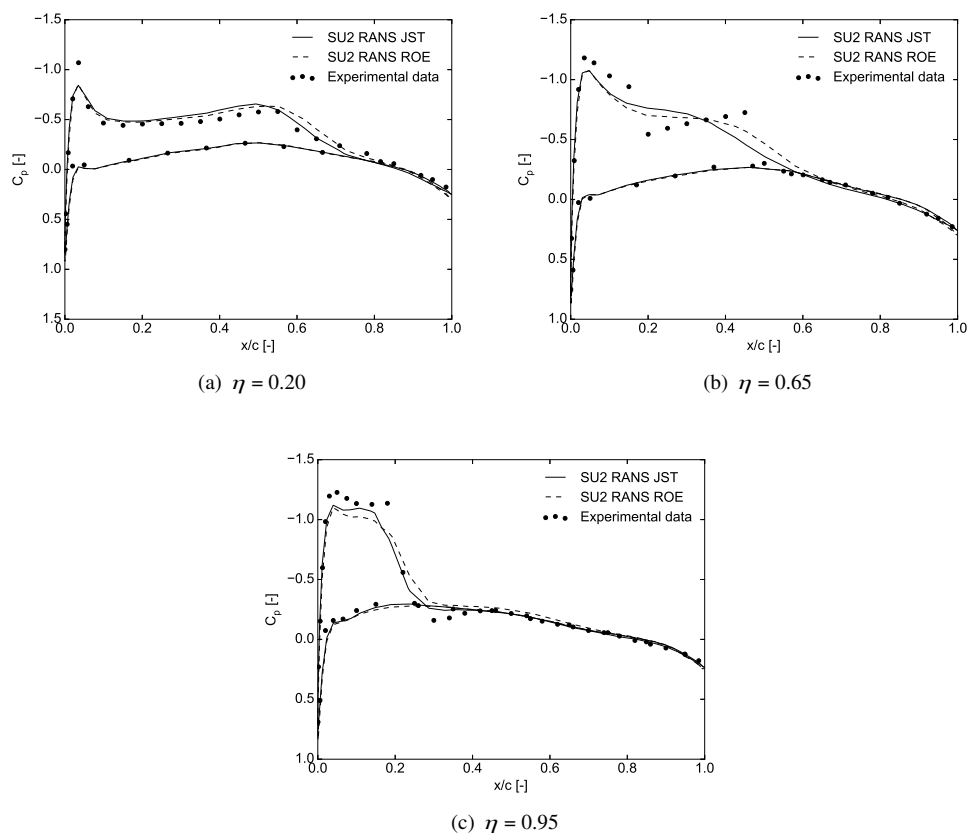
Fig. 20   SU2 RANS-SA solver validation using experimental data of the Onera M6 wing test 2308.

be attributed to the lower accuracy of the results of Crovato et al. as represented by the large relative error for the lift coefficient. Nonetheless, the order of magnitude and the direction of the pitching moment are similar. Overall, the agreement of the SU2 RANS-SA results with the experimental pressure data and the numerical aerodynamic coefficients is deemed satisfactory. Moreover, the JST numerical scheme provides sufficient accuracy while exhibiting favourable convergence behaviour as opposed to the more accurate but computationally demanding ROE scheme.

Table 3   SU2 RANS-SA solver aerodynamic coefficients validation using numerical data of the Onera M6 wing.

	Turb. model	C_L [-]	Rel. error C_L [%]	C_{D_p} [-]	C_{D_f} [-]	C_D [-]	C_m [-]
SU2 RANS JST	SA	0.255	1.29	127	53	180	-0.181
SU2 RANS ROE	SA	0.261	1.03	126	53	179	-0.180
Araya RANS [45]	SA	0.260	0.64	127	48	175	N/A
Araya RANS [45]	k-ω	0.262	1.42	128	51	179	N/A
Araya RANS [45]	SST	0.253	2.07	132	57	189	N/A
Le Moigne & Qin RANS [46]	Baldwin-Lomax	0.270	4.52	124	50	174	N/A
Nielsen & Anderson RANS [47]	SA	0.253	2.07	N/A	N/A	168	N/A
Crovato et al. RANS [48]	SA	0.272	5.29	N/A	N/A	181	-0.196

17

D. Optimisation Module Validation

The performance of the optimisation module of SU2 is verified by optimising the Onera M6 wing to reduce the drag coefficient. Similar constraints as outlined in Section II are imposed. These include a minimum thickness-to-chord ratio of 5.4% up to 7.7% for several predetermined wing sections, continuity constraints on the root and tip sections, and a fixed lift coefficient. An FFD box around the entire wing, similar to Figure 12, is used to define the 198 design variables. The optimisation converged after 23 designs, resulting in a reduction of 7.8% in the drag coefficient while satisfying the applied constraints. The effect of the optimisation is visualised in Figure 21, in which the cross-sectional shape and pressure distribution at $\eta = 0.50$ of both the original and the optimised design are visualised. The optimisation reduces the strength of the shock wave on the upper surface by adjusting the curvature of the airfoil on both the suction and pressure side. This test optimisation verifies the abilities of SU2 to effectively move towards a design which meets the objective and constraints. Furthermore, the sensitivity module is verified as the gradient-based optimiser shows the expected behaviour in the search for the optimum. More specifically, an overall decrease of the drag coefficient is observed, with several sudden increases as the optimiser tries to verify the descent direction by taking a step in a different direction. However, as the optimisation algorithm is gradient-based, there is no guarantee that the resulting optimum is a global optimum. It must be noted that this optimisation is conducted with a relatively coarse mesh as it is used to evaluate the performance and behaviour of the optimiser rather than obtaining an accurate design.

(a) Airfoil cross-section at $\eta = 0.50$. (b) C_P distribution at $\eta = 0.50$
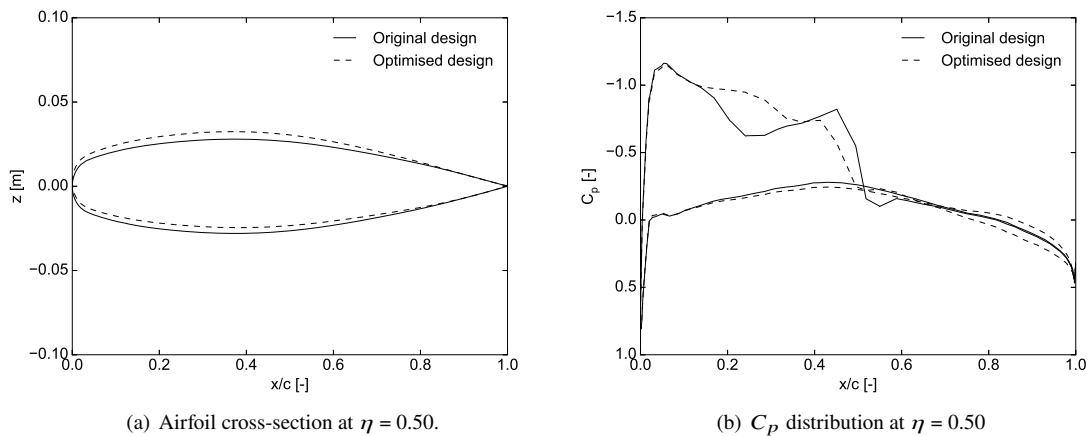
Fig. 21   SU2 optimisation verification using the Onera M6 wing.

IV. Results & Discussion

After the complete optimisation structure is implemented and validated, the aerodynamic shape optimisation of the Flying V outboard wing is conducted. The optimisation is performed at a single design point, in particular the cruise condition. Following the drag polar obtained by Oosterom [16], and the Mach number of 0.85 as prescribed by top-level requirements, the lift coefficient at the design condition is 0.26 at a cruise altitude of 11 km. During the flow analysis, the angle of attack corresponding to this lift coefficient is found iteratively and is, therefore, an additional result of the optimisation.

As an Euler-based optimisation process and RANS flow analyses are computationally demanding, the analyses are conducted on a High-Performance Computing (HPC) cluster. This enables the process to run in parallel by being distributed over 48 to 80 cores, amounting to at least 192 GB of memory on either an AMD Opteron or Intel Xeon processor. The gradient-based optimisation is terminated after 100 iterations or when the change in objective function between iterations is smaller than 1×10^{-5}. On the other hand, the Euler analyses are limited to 750 iterations as it is found that most designs converge within this range to a maximum root-mean-square error of 10^{-8} for the flow properties. Furthermore, the baseline optimisation is distributed over 8 cores on a local notebook with an Intel Xeon processor including 8 GB memory. The results of the optimisation process are summarised in Table 4, and Figures 22, 23 and 24. The steps visualised in Figure 9 are discussed in the following sections.

Table 4   Aerodynamic coefficients and angle of attack for designs (0) to (4) at $Re = 1.135 \times 10^8$ and $M = 0.85$.

Design	Flow model	C_L [-]	α [°]	C_D [-]	C_{D_p} [-]	C_{D_f} [-]	C_m [-]	C_L/C_D [-]
Linear Design (0)	RANS-SA	0.260	2.6	146	63.6	82.0	0.035	17.9
Initial Design (1)	RANS-SA	0.260	2.0	122	75.9	45.6	0.038	21.4
Baseline Design (2)	RANS-SA	0.260	2.2	136	90.3	45.9	0.044	19.1
Baseline Design (2)	Euler+	0.260	1.6	136	N/A	N/A	0.069	19.1
Single Step Design (3)	Euler+	0.260	1.2	128	N/A	N/A	0.074	20.3
Dual Step Design (4)	Euler+	0.260	1.4	134	N/A	N/A	0.071	19.4

(a) Maximum C_L/C_D versus C_L

(b) Drag polar
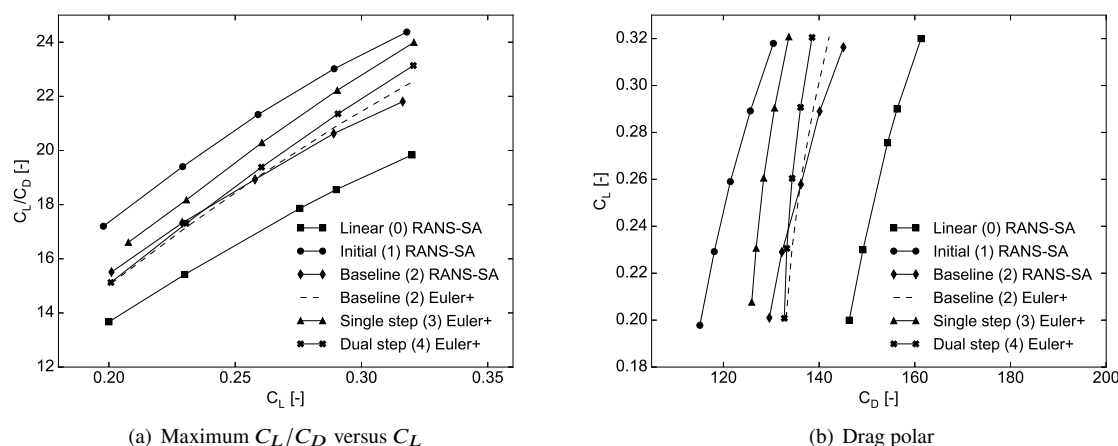
Fig. 22   Aerodynamic performance of designs (0) to (4) at $Re = 1.135 \times 10^8$ and $M = 0.85$.

19

(a) Linear design (0)   (b) Initial design (1)   (c) Baseline design (2)
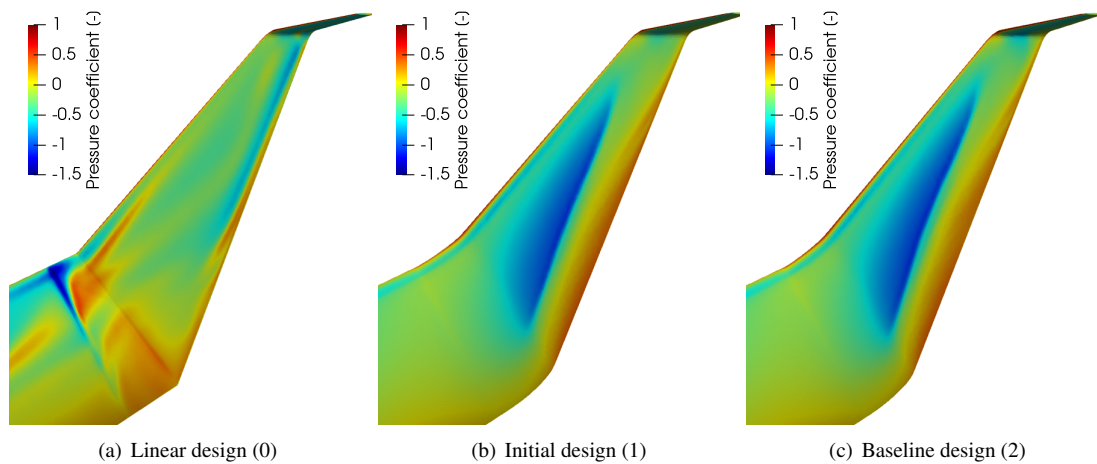
Fig. 23 SU2 RANS-SA outer wing upper surface pressure distributions of the linear (0), initial (1) and baseline (2) designs at $Re = 1.135\text{x}10^8$, $M = 0.85$, and $C_L = 0.26$ with $\overline{c} = 17.7$ m.

(a) Baseline design (2)   (b) Single step design (3)   (c) Dual step design (4)
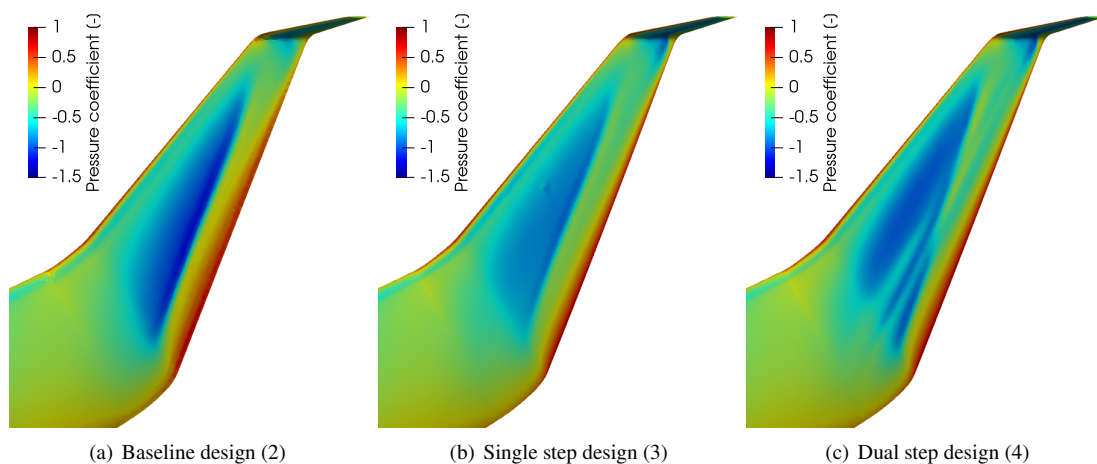
Fig. 24 SU2 Euler outer wing upper surface pressure distributions of the baseline (2), single (3) and dual step (4) designs at $M = 0.85$, and $C_L = 0.26$ with $\overline{c} = 17.7$ m.

20

A. Flow Model Correlation

To be able to compare the results of designs (0) to (4), a correlation between the SU2 RANS-SA and the Euler+ models needs to be found. To do so, *baseline design (2)* is analysed with both models as well as with additional SU2 RANS models augmented with various turbulence models. The turbulence models considered include Menter's SST model and the SA-E model as incorporated in SU2. The results are summarised in Table 5. Additionally, the drag polar for *baseline design (2)* is constructed using both the SU2 RANS-SA and Euler+ model as visualised in Figure 22. The variation in the drag coefficient obtained by the SU2 RANS analyses amounts to 1.5 drag counts which equals 1.1% of the average drag. Similarly, the variation in the lift-to-drag ratio amounts to 1.1%. The error in the pitching moment coefficient is slightly larger and equals 2.3% of its average value. This larger value originates from the fact that the value of the pitching moment itself is small, hence relative errors are larger.

As the variation in the results of the SU2 RANS analyses is considered acceptable, the Euler+ model is compared to the SU2 RANS-SA model as the latter is also used to construct the data in Table 4. It is expected that the drag coefficient of the Euler+ model is underestimated since the viscous drag component is approximated using the empirical module of Faggiano [12]. This is confirmed by the results in Table 5. The drag coefficient of the Euler+ model is 3.9 drag counts lower than that of the RANS-SA model, amounting to an error of 2.9%. The lift-to-drag ratio is directly related to this error, hence its value is overestimated by approximately 2.9%, as seen in Figure 22. Whereas the Euler+ model closely resembles the RANS-SA model for lower lift coefficients, its deviation increases as the lift coefficient increases, indicating that the model is not reliable for lift coefficients beyond the design condition. As the error of the drag coefficient of the Euler+ model is known, the difference of 3.9 drag counts is added to the results of the model resulting in the drag values shown in Table 4 and Figure 22.

Moreover, the required angle of attack is severely underestimated as seen in Table 5, meaning that the Euler+ model overestimates the lift curve slope. Also, the pitching moment coefficient is overestimated by the Euler+ model, with an error of 0.025 which equals more than 50%. This large difference can be attributed to the fact that the Euler equations overestimate the strength of suction areas. The actual pitching moment coefficient is therefore closer to zero than what is predicted by the Euler+ model. This means that the aircraft is also closer to its trim condition and thus smaller control surface deflections are required to reach it, resulting in less trim drag. While the Euler+ model provides a good insight into the overall aerodynamic efficiency of the aircraft at its design condition, care should be taken when considering other flight conditions and when interpreting the pitching moment coefficient.

Table 5   Aerodynamic coefficients and angle of attack of baseline design (2) for various SU2 RANS turbulence models and the Euler+ model at $Re = 1.135 \times 10^8$ and $M = 0.85$.

| Flow Model	C_L [-]	α [°]	C_D [-]	C_m [-]	C_L/C_D [-]
RANS-SA	0.26	2.2	136.2	0.044	19.08
RANS-SA-E	0.26	2.3	137.1	0.043	18.96
RANS-SST	0.26	2.1	135.6	0.044	19.17
Euler+	0.26	1.6	132.3	0.069	19.65

B. Geometry Preparation: Linear Design (0) to Initial Design (1)

The first step of the design process is to adjust the geometry with the new lofting technique explained in Section II. The change in the cross-sectional shape at different spanwise locations is visualised in Figure 25 together with the obtained pressure distributions. Additionally, the complete upper surface pressure distributions are visualised in Figures 23a and 23b. In Figure 25a it is observed that the new lofting technique removes the kinks in the streamwise direction, which is also reflected by the elimination of the shock waves on the upper and lower surface where these discontinuities occurred. Moreover, by eliminating section 4 from the planform parametrisation, the change from oval section 3 to the transonic airfoil of section 5 is spread out over the entire span of the outboard wing, leading to a more gradual change in the cross-sectional shape. This gradual change does however result in a significantly thicker outboard wing, even at more outboard located sections as seen in Figure 25b.

The thickness of the wing in combination with the transonic flight condition results in shock waves on both the upper and lower surface as can be seen in Figures 25 and 23b. The large thickness-to-chord ratio and resulting curvature lead to high supervelocities, which in turn result in shock waves. The increased leading edge radius of the outboard

wing sections also results in a larger leading edge suction peak compared to *linear design (0)*. Note however that the shock visualised in Figure 25b is a normal shock wave. When looking at the Mach number in front of the shock and the Normal Shock Relations of Anderson [49], it is expected that the Mach number behind the normal shock wave would be lower with respect to C_p^* than what is predicted by the SU2 RANS-SA model. This discrepancy can be attributed to the reduced accuracy of the SA turbulence model when shock wave/boundary layer interaction flows are present [50].

The pressure distributions of *initial design (1)* additionally suggest that little lift is generated on the outboard wing. This is verified by the spanwise lift distribution shown in Figure 26. While *linear design (0)* exhibits strong shock waves at the streamwise discontinuities, it produces a fairly elliptical lift distribution as opposed to the lift distribution of *initial design (1)*. The latter exhibits a large drop in the generated lift at $\eta = 0.60$, this location corresponds to the thickest point of the outboard wing. The decreased efficiency of the wing is also reflected by the difference in the sectional lift coefficient for *linear design (0)* and *initial design (1)*. Nonetheless, the aerodynamic performance of *initial design (1)* is significantly improved as seen in Table 4. This is also seen in the upper surface pressure distribution as there is a more gradual change in pressure coefficient at the transition location of the inboard and outboard wing, as seen in Figures 23a & b. The Gordon surfaces lofting technique thereby increases the lift-to-drag ratio by 19.6%. The aerodynamic performance is further visualised in Figure 22 where it is observed that *initial design (1)* notably outperforms *linear design (0)* over the entire range of operating conditions.


(a) $\eta = 0.60$

(b) $\eta = 0.80$
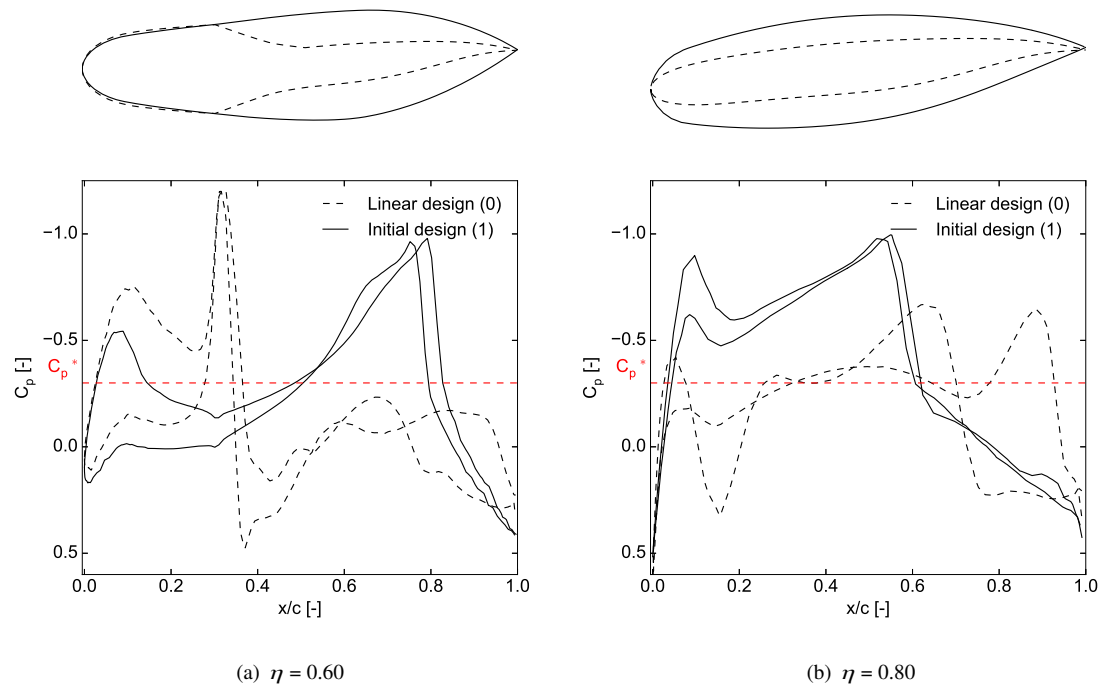
Fig. 25 RANS-SA pressure coefficient and airfoil section of the linear (0) and initial (1) design at C_L = 0.26, *Re* = 1.135x10^8, M = 0.85 and C_p^* = -0.30.

(a) Lift coefficient distribution

(b) Lift distribution
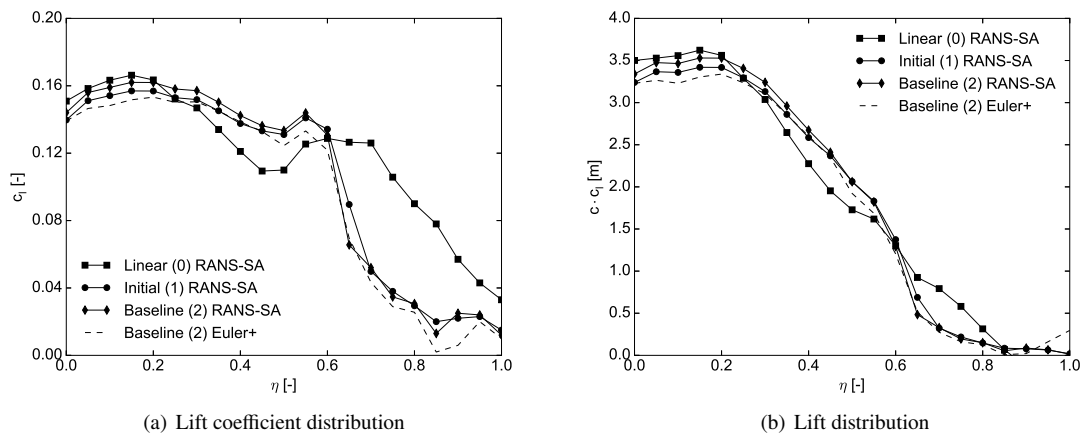
Fig. 26 **Spanwise lift and lift coefficient distribution for the linear (0), initial (1) and baseline (2) design at C_L = 0.26, Re = 1.135x10^8 and M = 0.85.**

As the RANS equations describe the viscous boundary layer effects as well, both the pressure and friction drag components are obtained. Looking at Table 4, it is observed that the pressure drag is increased for *initial design (1)*. This can be explained by considering the pressure distributions shown in Figure 25. As the thickness and curvature of the wing are increased, the shock waves move aft, which increases their strength as well as the aft suction originating from the higher supervelocities. This finally leads to a higher pressure drag. On the other hand, the friction drag component is reduced remarkably according to the numerical results. This is however unexpected as the wetted areas of *linear design (0)* and *initial design (1)* are not significantly different. After further investigation, it is found that the prism layers in the mesh of *linear design (0)* are distorted. This can be ascribed to the unfavourable geometry of the design. The torus section in combination with the kinks in the planform and the cross-sectional shapes leads to a surface mesh with a lower quality, which is translated to the prism layers. This effect is also seen in the friction coefficient distributions shown in Figure 27, where the distributions for *linear design (0)* exhibit nonphysical behaviour.

(a) η = 0.60

(b) η = 0.80
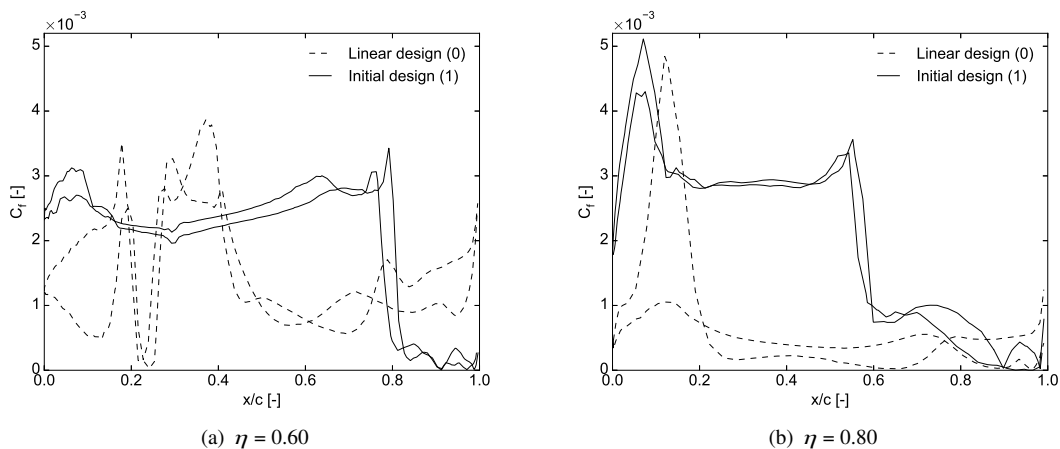
Fig. 27 **SU2 RANS-SA friction coefficient of the linear (0) and initial (1) design at C_L = 0.26, Re = 1.135x10^8 and M = 0.85.**

In contrast, the behaviour of the friction coefficient of *initial design (1)* can be explained by physical phenomena. The friction coefficient remains fairly constant up until the shock waves near x/c = 0.80 and x/c = 0.60 for η = 0.60 and η = 0.80 respectively. The friction coefficient moves towards zero after the shock waves occur, however, no recovery of

the friction coefficient is observed afterwards. This can indicate trailing edge flow separation, which increases the drag due to the low pressure wake that is created behind the wing. Lastly, the pitching moment coefficient of *initial design* (1) is increased compared to *linear design (0)*. This can be explained by the large suction area on the nose of *initial design (1)* due to the cockpit integration, as was found by Brouwer [14]. This is to be compensated by higher control surface deflections when trimming the aircraft, leading to a larger trim drag component.

C. Baseline Design Optimisation: Initial Design (1) to Baseline Design (2)

The baseline design optimisation aims to efficiently move towards an optimised planform design which serves as input to the FFD shape optimisation. As discussed in Section II, additional design goals are integrated into this process. These changes are expected to degrade the aerodynamic performance as the changes result in a thicker and more voluminous wing not corresponding with the design goals of transonic wings. The optimisation guided by the DE algorithm starts with a population size of five times the number of design variables and is terminated whenever the optimiser does not converge within 50 iterations. The baseline design follows from the optimisation process after 32 generations and 10 hours of computational time. The resulting planform variables are shown in Table 6.

It is observed that the optimised taper ratio is equal to the lower bound determined by the design changes, which confirms that a higher taper ratio is not beneficial. Additionally, a smaller outboard wing sweep angle in combination with a more negative tip incidence angle is found by the optimiser. The larger incidence angle directly translates to the objective of obtaining an elliptical lift distribution, while the adjusted sweep angle in combination with the change in b and L_4 accounts for the imposed reference area constraint. As the resulting reference area is only increased by 1.4 m², it can be said that the wing loading, and thus the low-speed characteristics of the aircraft, remain intact. Next to the Euler flow analysis, the baseline design check also includes the sizing of the outboard control surfaces. The requirement imposed on the size of the control surfaces follows from the scale model used in sub-scale flight testing. These flight tests demonstrated that the required control surface area of a single wing half should equal approximately 27.85 m² to full fill controllability requirements [26]. After analysing both *initial design (1)* and *baseline design (2)*, it is found that the control surface area increases when the maximum allowed offset between the hinge line and camber lines increases as well. As this is not beneficial, the lowest possible offset resulting in the minimum required surface area must be found. This yields the maximum offsets and control surface areas shown in Table 6, and Figure 28. The maximum offset is found near the leading edge sweep angle change. The geometry in the vicinity of this sweep angle change is complex and therefore more likely to exhibit a larger hinge line offset.

Table 6   Planform design variables and optimisation metrics for the initial (1) and baseline (2) design.

Parameter	Unit	Initial design (1)	Baseline design (2)
b	m	14.75	14.65
Λ_{out}	°	40.70	39.57
λ	-	0.10	0.12
L_4	m	1.50	1.18
δ	°	1.00	1.04
ϵ_5	°	-4.37	-5.48
S_{ref}	m²	875.31	876.74
δs_{max}	cm	10.97	8.86
S_{con}	m²	27.59	27.75

While the control surface design for *baseline design (2)* is more accurate due to its lower maximum offset, the aerodynamic performance of the aircraft compared to *initial design (1)* is inferior. This can be seen in Table 4 and Figure 22. The lift-to-drag ratio is decreased by 10.7% as the pressure drag component increased. This increase in pressure drag is caused by the stronger shock waves which extend more outboard, as seen in Figures 29, 30 and 23 respectively. This can be attributed to the larger thickness of the wing due to the change in the airfoil profile of section 5. The shock wave strength is increased most distinctly in the outboard regions of the wing as the thickness change there is more pronounced, see Figure 29b. The stronger shocks also cause a higher chance of trailing edge flow separation as the friction coefficient approaches zero increasingly as seen in Figure 30b. The friction drag itself grew slightly as well.

24
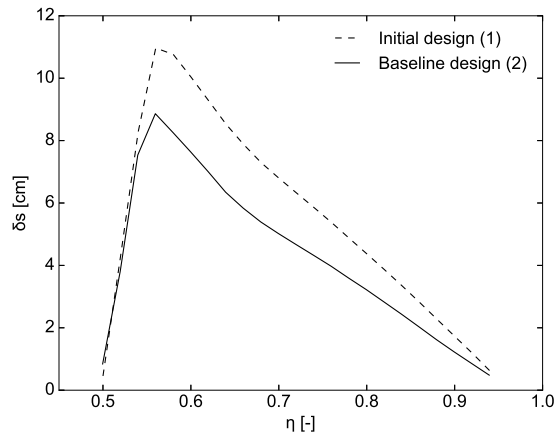
Fig. 28   Hinge line offset w.r.t. the camber line at various spanwise locations for the initial (1) and baseline (2) design.

This can be attributed to the small increase in the wetted area resulting from the increase in the taper ratio. Finally, the objective of the automated baseline optimisation is to obtain an elliptical lift distribution. From Figures 26 and 29 it can, however, be seen that *baseline design (2)* does not have a more efficient outboard wing than *initial design (1)*. This can be attributed to the incorporated design changes and their negative effect on the aerodynamic performance of the aircraft.

(a) $\eta = 0.60$
(b) $\eta = 0.80$
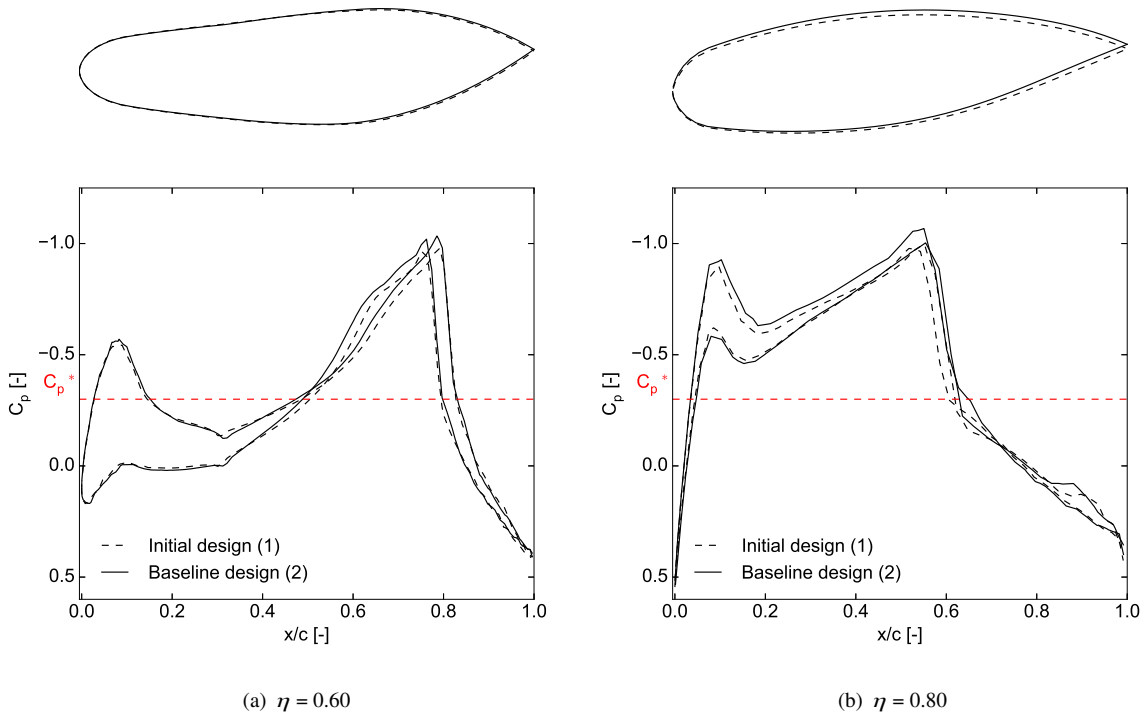
Fig. 29   SU2 RANS-SA pressure coefficient and airfoil section of the initial (1) and baseline (2) design at C_L = 0.26, Re = 1.135x10^8, M = 0.85, and C_p^* = -0.30.

25

(a) $\eta = 0.60$

(b) $\eta = 0.80$
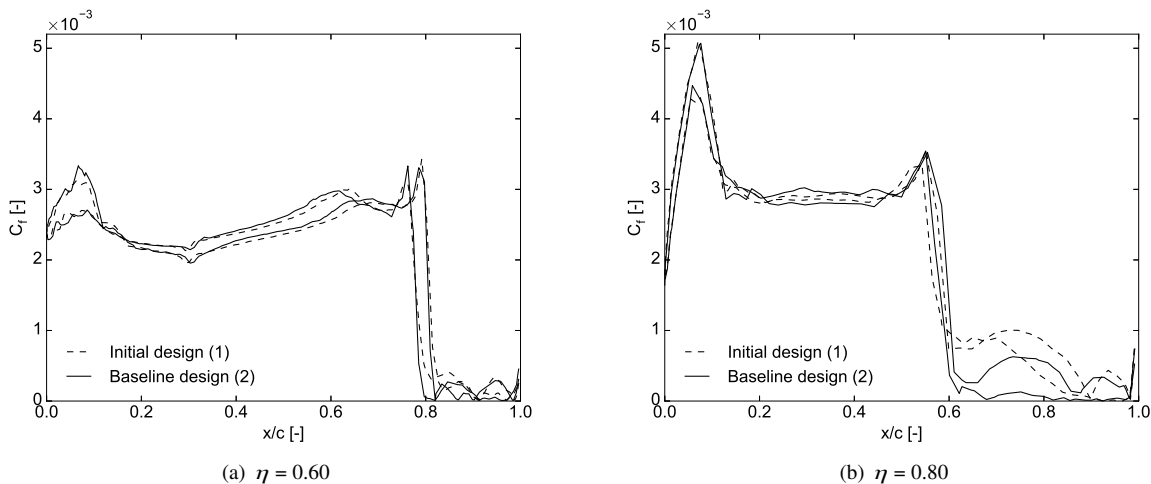
Fig. 30   SU2 RANS-SA friction coefficient of the initial (1) and baseline (2) design at C_L = 0.26, Re = 1.135x10^{8} and M = 0.85.

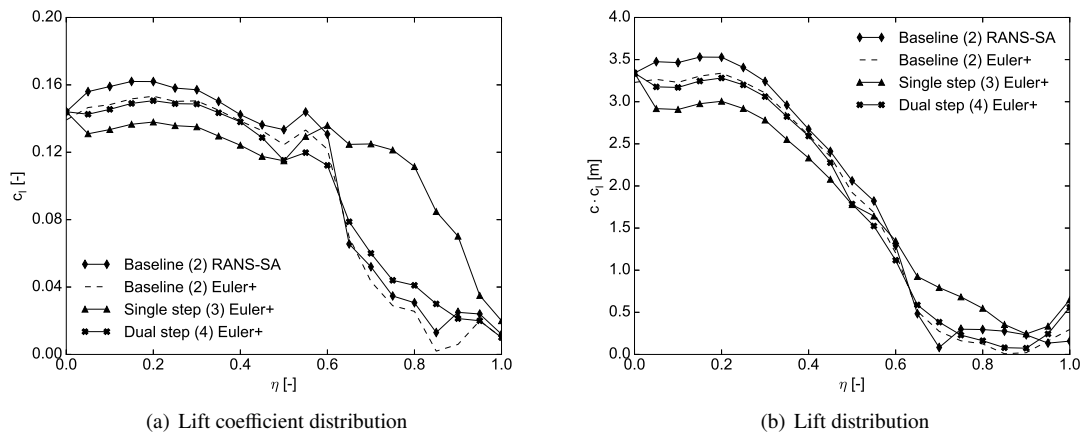## D. Single Step Optimisation: Baseline Design (2) to Single Step Design (3)

The goal of the single step FFD optimisation is to increase the lift-to-drag ratio which is degraded due to the design changes incorporated in *baseline design (2)*. The control surface integration is not considered during this optimisation, meaning that all control points except the ones located near the root and tip section of the FFD box are allowed to move. As the FFD box consists of 12 control points in both the *x* and *y* direction, and 2 in the *z* direction, the total number of control points free to move amounts to 240. The number of control points is based on a trade-off between the design flexibility and computational cost [51–53]. A total of 22 design iterations are conducted in 6.5 hours. This results in *single step design (3)* with a lift-to-drag ratio of 20.3, adding up to an increase of 6.3% compared to *baseline design (2)* as analysed by the Euler+ model. The aerodynamic performance is further shown in Table 4 and Figure 22. The increase in the lift-to-drag ratio is also reflected in the required angle of attack during cruise. *Single step design (3)* requires an angle of 1.2°while *baseline design (2)* requires an angle of 1.6°according to the Euler+ model. A lower angle of attack in cruise is desired as this implies that a lower angle of attack can be attained during landing, resulting in a shorter landing gear length, and thus reduced weight.

The improvement in aerodynamic efficiency can be attributed to the decrease in shock wave strength on the upper surface. This can be seen in Figures 24 and 31. The change in the cross-sectional shape causes a lower curvature of the upper surface resulting in lower supervelocities, and thus a reduced shock wave strength. This applies to the upper surface shock waves present at $x/c = 0.78$ and $x/c = 0.60$ for $\eta = 0.60$ and $\eta = 0.80$ respectively. The decrease in shock wave strength also results in a more nose-up pitching moment as the suction area on the nose of the aircraft becomes relatively stronger. It is however observed that the shock wave strength on the lower surface is increased slightly, most notably in the inboard sections. Furthermore, a lambda shock is present on the lower surface which is also captured in Figure 31b at $x/c = 0.60$ and $x/c = 0.80$.

As seen in Figure 32, the sudden loss of lift on the wing of *baseline design (2)* is removed and a more elliptical lift distribution is obtained for *single step design (3)*. This can be ascribed to the change in the incidence angle of the airfoil sections as indicated by the trailing edge movement of the cross-sections visualised in Figure 31. The FFD optimisation is more efficient in obtaining an elliptical lift distribution than the automated baseline optimisation as it has more design flexibility to overcome the negative effects of the increase in thickness of the wing. The more efficient outboard wing in combination with the reduced upper surface shock wave strength thereby results in a more favourable aerodynamic performance for *single step design (3)*.

(a) $\eta = 0.60$

(b) $\eta = 0.80$
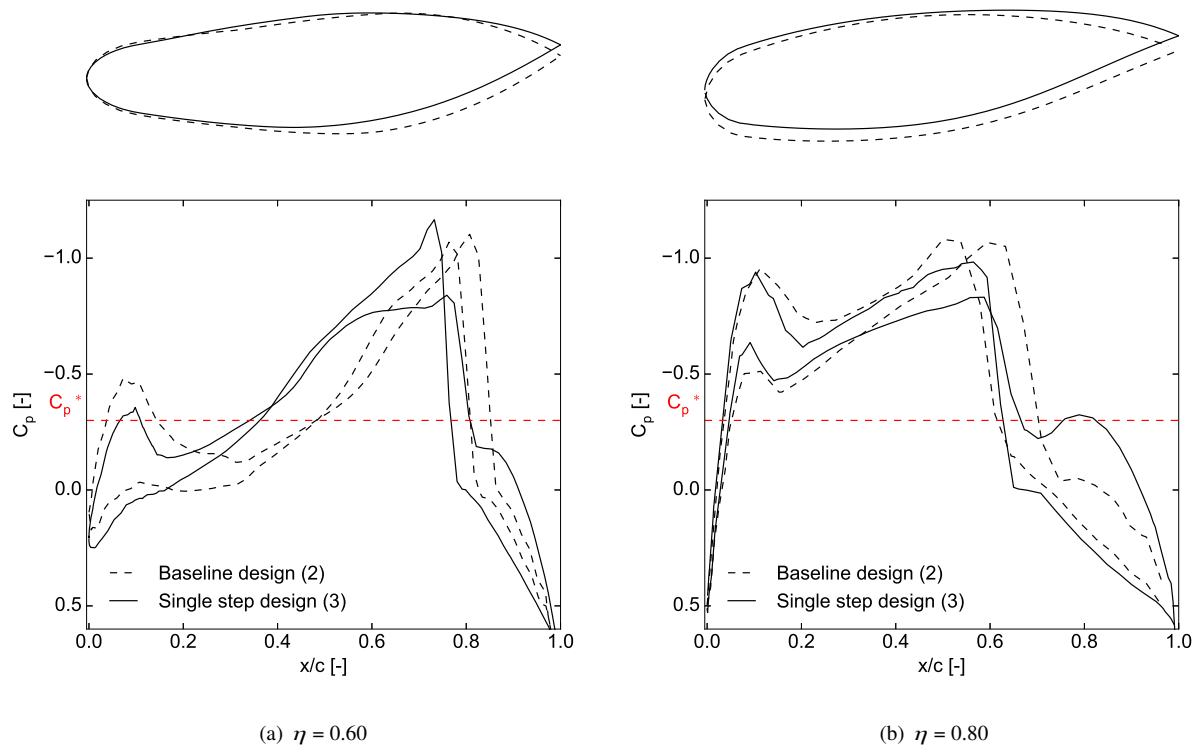
Fig. 31   SU2 Euler pressure coefficient and airfoil section of the baseline (2) and single step (3) design at C_L = 0.26, M = 0.85, and C_p^* = -0.30.



(a) Lift coefficient distribution

(b) Lift distribution

Fig. 32   Spanwise lift and lift coefficient distribution for the baseline (2), single (3) and dual step (4) design at C_L = 0.26 and M = 0.85.

E. Dual Step optimisation: Baseline Design (2) to Dual Step Design (4)

A more complete picture of the potential aerodynamic performance of the Flying V is obtained by considering the integration of the outboard control surfaces. This integration constraint results in the use of two FFD boxes. Both are described by 12 control points in the x and y direction and 2 in the z direction, similar to the FFD box used in the single step optimisation. After the control surface sizing, the optimisation of the wing in front of the hinge line is conducted. As the plane in which the hinge line is located is fixed as well, the number of free control points reduces to 220. These points are optimised through 30 design iterations taking a total of 7.5 hours. Subsequently, the area aft of the hinge line is optimised using the same number of control points as the same number of planes is fixed. This second step of the optimisation consists of 28 design iterations in 5.8 hours. The resulting *dual step design (4)* exhibits an aerodynamic efficiency of 19.4, which is an increase of 1.6% compared to *baseline design (2)* as analysed by the Euler+ model. Additionally, the angle of attack required in cruise is reduced from 1.6°to 1.4°, resulting in the weight benefits related to the landing gear design.

The small increase in aerodynamic efficiency can be ascribed to the hinge line constraint as this prohibits the cross-sectional shape from changing significantly. Its effect can best be seen in Figure 33b at $x/c = 0.65$. The constraint also prevents large movements of the trailing edge, leading to less design freedom to attain a favourable lift distribution. This is verified by Figure 32 in which it is observed that the efficiency of the outboard wing is only slightly increased compared to *baseline design (2)*. The restricted movement of the control points also prevents the optimiser from efficiently reducing the strength of the shock waves. On the upper surface of the inboard sections, this results in additional shock waves as captured in Figures 33a and 24c at $x/c = 0.75$ and $x/c = 0.85$. Also, a strong lambda shock on the lower surface is observed at $x/c = 0.80$ in Figure 33b. Nonetheless, the overall strength of the shock waves on the outboard wing is slightly reduced compared to *baseline design (2)* due to the notably weaker upper surface shock waves. This is further supported by the slightly increased pitching moment coefficient of *dual step design (4)* shown in Table 4. The large suction area on the nose of the aircraft becomes relatively stronger as the suction on the outboard wing becomes less, resulting in a larger nose-up pitching moment. This increase can lead to additional trim drag as larger control surface deflections are needed to trim the aircraft.

(a) $\eta = 0.60$ (b) $\eta = 0.80$
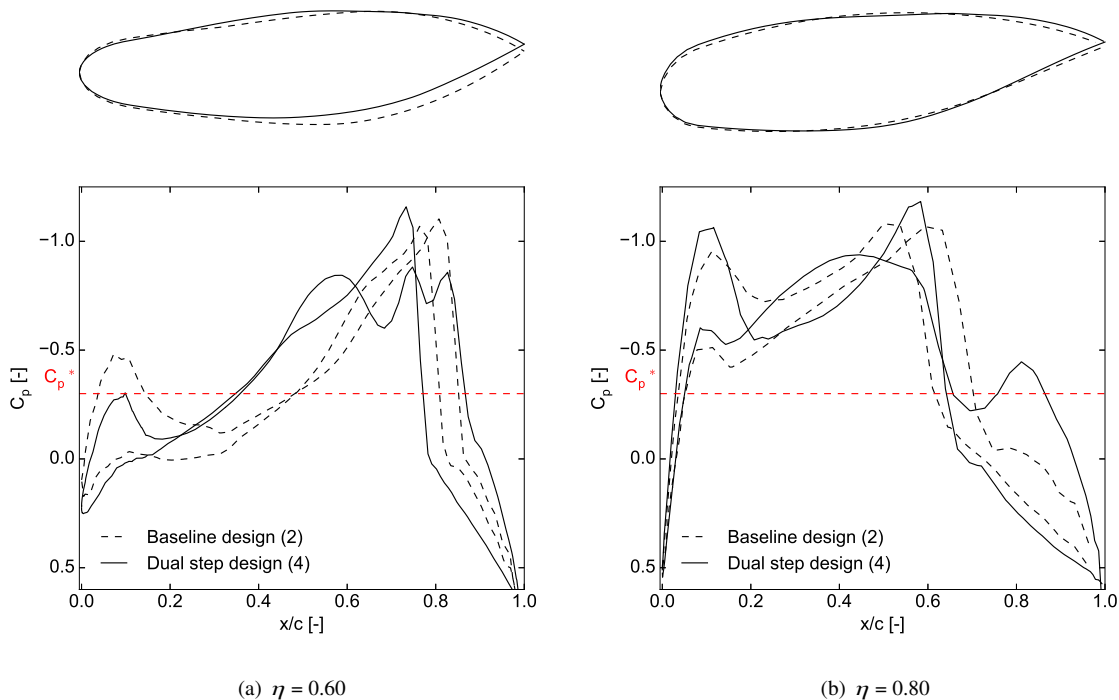
Fig. 33 **Euler pressure coefficient and airfoil section of the baseline (2) and dual step (4) design at $C_L = 0.26$, $M = 0.85$ and $C_p^* = -0.30$.**

F. Overall Design Comparison

After evaluating the effect of the various design steps, the overall performance of all designs can be compared. While the single step FFD optimisation improves the aerodynamic efficiency by 6.3% compared to *baseline design (2)*, there is no improvement when comparing its performance against *initial design (1)*. The lift-to-drag ratio of *single step design (3)* is 5.4% lower than the efficiency of *initial design (1)*. This furthermore supports the statement that introducing a higher thickness-to-chord ratio for the tip airfoil as well as increasing the taper ratio, is detrimental to the aerodynamic performance of the aircraft. Even though the aerodynamic performance has deteriorated, the decrease in the angle of attack can have a significant impact on the aircraft design. The required angle of attack in cruise for *single step design (3)* is 0.8°lower than the angle needed for *initial design (1)*. It must however be noted that the Euler+ model overestimates the lift curve slope so the actual decrease in the angle of attack is smaller. Nonetheless, even a small decrease in the angle of attack can result in a reduced weight for the landing gear. *Single step design (3)* also outperforms *initial design (1)* when considering the lift distribution in Figures 26 and 32. Whereas *single step design (3)* produces a relatively elliptical lift distribution, *initial design (1)* has a very inefficient outboard wing design which produces little lift due to the shock waves on both the upper and lower surface.

Dual step design (4) is also outperformed by *initial design (1)* as its aerodynamic efficiency is 9.3% lower. This is because the optimiser is constrained by the integration of the control surfaces, making it unable to devise a significantly more efficient outboard wing for *dual step design (4)*. Therefore, only a small increase in the outboard wing efficiency is observed in Figure 32. The results also show that the lift-to-drag ratio of *dual step design (4)* is 4.4% lower than the lift-to-drag ratio of *single step design (3)*. This directly implies that the integration of the control surface design has a non-negligible impact on the resulting aerodynamic performance. The control surface integration limits the design flexibility by freezing an additional plane in the spanwise direction of the wing. As a continuity constraint is imposed on this plane, additional control points in the vicinity of this plane are not allowed to move as well. This prohibits the optimiser from adjusting the surface curvature as well as the trailing edge position sufficiently. So, among all designs, only *initial design (1)* reaches the Flying V lift-to-drag target ratio of 20.5 as found by Oosterom and Vos [54]. Nonetheless, *single step design (3)* approaches it, and as only the outboard wing of the aircraft is optimised, there is a possibility to meet this requirement when the inboard wing and winglets are optimised as well.

Another point of attention is the pitching moment coefficient of all designs. While the FFD optimisation imposes a constraint on the maximum and minimum pitching moment coefficient, none of the designs attains this strict constraint. This can be attributed to the large area of suction on the nose of the aircraft. Following from Section IV.A, it must be noted that the pitching moment coefficients of *single step (3)* and *dual step design (4)* are overestimated by 0.025. Hence, the nose-up pitching moment is expected to be smaller, resulting in lower required control surface deflections and thus less trim drag than expected from the values listed in Table 4. The remaining nose-up pitching moment can be neutralised to zero by shifting the centre of gravity forward without harming the stability margin. However, more outboard loading may also decrease the pitch-up tendency of the aircraft, as well as improve the lift distribution at the same time. Overall, *initial design (1)* outperforms all designs in terms of aerodynamic efficiency, whereas *single step design (3)* exhibits the most favourable lift distribution. It is clear that the integration of the design changes and the outboard control surfaces limit the design flexibility of the optimiser and thereby degrade the aerodynamic performance of the aircraft significantly.

Table 7   Zero lift drag coefficient and Oswald efficiency factor for designs (0) up to (4).

Design	Flow model	C_{D_0} [-]	S_{ref} [m^2]	AR [-]	e [-]	$(\frac{C_L}{C_D})_{\max}$ [-]	$C_{L_{\text{opt}}}$ [-]
Linear Design (0)	RANS-SA	79.9	875.1	4.83	0.673	17.9	0.29
Initial Design (1)	RANS-SA	75.6	875.1	4.83	0.965	22.0	0.33
Baseline Design (2)	RANS-SA	76.2	876.5	4.82	0.732	19.1	0.29
Baseline Design (2)	Euler+	76.2	876.5	4.82	0.746	19.3	0.29
Single Step Design (3)	Euler+	76.7	876.5	4.82	0.867	20.7	0.31
Dual Step Design (4)	Euler+	76.4	876.5	4.82	0.773	19.6	0.30

For further comparison of the designs, the Oswald efficiency factor is determined based on the zero-lift drag component found by the empirical viscous drag module of Faggiano [12], in combination with the total drag coefficient collected in Table 4. The results are summarised in Table 7. It is observed that *initial design (0)* exhibits the highest Oswald efficiency factor followed by *single step (3)* and *dual step design (4)*. Based on the Oswald efficiency factor, the expected maximum lift-to-drag ratio can be found, as well as the lift coefficient at which this is attained. It must be noted that the values obtained using the Oswald efficiency deviate from the values recorded in the drag polar curves of Figure 22. Contrary to what is expected, the drag polar curves do not show a maximum lift-to-drag ratio, indicating that the aircraft can fly at higher lift coefficients than assumed before. This unexpected behaviour can be attributed to the fact that no 3D effects are modelled in SU2 while they can influence the resulting lift and drag coefficients, especially when separation occurs [55]. As all designs experience a local Mach number higher than 1.3 at high lift coefficients, shock-induced separation is expected and 3D effects can become more pronounced. Additionally, the chosen turbulence model also affects how the separation is captured, as it is known that the SA turbulence model is not very accurate when shock wave/boundary layer interaction flows occur [50, 55]. Hence, the drag polar shown in Figure 22 is assumed to be inaccurate at higher lift coefficients, and the actual maximum lift-to-drag ratio of the designs is expected to be closer to the values listed in Table 7. The latter values also indicate that the aircraft is more efficient at a higher cruise lift coefficient than the assumed design lift coefficient of 0.26.

G. Parameter Sensitivity Study

As the thickness of the outboard wing is still significant after the FFD shape optimisations, it is decided to conduct a parameter sensitivity study into the effect of reducing the thickness of oval section 3. As the root of the outboard wing is constrained by this section, a thinner oval section can result in a thinner outboard wing as the thickness change between section 3 and section 5 is less. It must be noted that the shape of section 3 is dictated by top-level requirements related to the placement of cargo containers, meaning that decreasing the thickness of the oval section results in a violation of these requirements. The thickness of the oval section is determined by three variables: the crown height H_1, the oval cabin height H_2 and the keel height H_3 as visualised in Figure 34. By decreasing the keel and crown height, parameter study design 1 is formed, while decreasing the oval cabin height results in parameter study design 2. To compare the resulting designs, *baseline design (2)* is chosen as a reference.

The designs are analysed using the SU2 RANS-SA model. The resulting aerodynamic coefficients together with the oval cabin parameters are shown in Table 8. The effect of the decreased thickness on the streamwise airfoil profile at $\eta = 0.60$ is visualised in Figure 35. Decreasing the total section thickness by 9.4% in parameter study design 1 leads to an increase of 0.94% in the lift-to-drag ratio. Whereas decreasing the thickness via the oval cabin height by 4.7% results in an increase of 0.37%. A slight decrease in friction drag is observed for parameter study design 1 & 2 as the wetted area is reduced by a small amount due to the less curved upper and lower surface. Following the results, it is determined that reducing the thickness by adjusting the keel and crown height is the most effective in increasing the lift-to-drag ratio. This is because it results in a less curved upper and lower surface leading to lower supervelocities and thus a weaker shock wave. Nonetheless, the increase in aerodynamic efficiency is very small and therefore makes violating top-level requirements less attractive.

Table 8   Oval section 3 design parameters and SU2 RANS-SA aerodynamic coefficients at $C_L = 0.26$, $Re = 1.135 \times 10^8$ and $M = 0.85$.

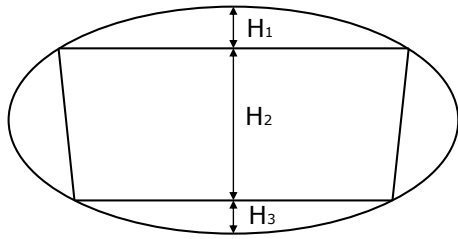| Design	H_1 [m]	H_3 [m]	H_2 [m]	α [°]	C_D [-]	C_{D_p} [-]	C_{D_f} [-]	C_m [-]	C_L/C_D [-]
Baseline Design (2)	0.45	0.45	1.22	2.2	136.2	90.3	45.9	0.044	19.08
Parameter study 1	0.35	0.35	1.22	2.2	135.0	89.5	45.5	0.043	19.26
Parameter study 2	0.45	0.45	1.12	2.2	135.8	90	45.8	0.044	19.15

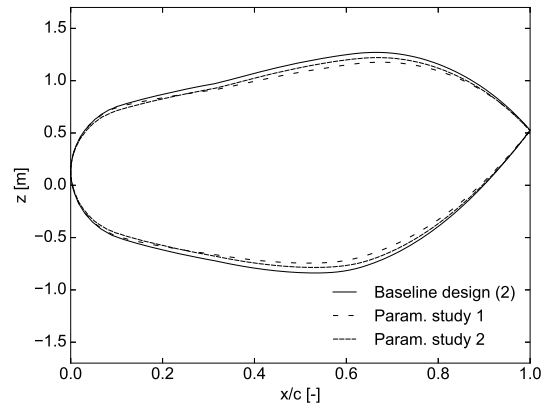**Fig. 34 Oval cabin parametrisation by Hillen [17].**

Fig. 35 Cross-sectional shape at $\eta = 0.60$ for baseline design (2), and parameter study designs 1 and 2.

V. Conclusion & Recommendations

The goal of this study is to design the outboard wing of the Flying V to maximise the lift-to-drag ratio in cruise conditions. This design is obtained through a change in lofting technique to form the geometry, followed by a constrained aerodynamic shape optimisation based on the Free-Form Deformation (FFD) parametrisation approach. Relevant constraints include, among others, a range of acceptable pitching moment coefficients, and the integration of the outboard control surfaces. The maximal lift-to-drag ratio of the aircraft after the FFD optimisation is found to be 19.4 in cruise conditions. An additional FFD optimisation is performed in which the control surface integration is neglected. This optimised design results in an aerodynamic efficiency of 20.3, indicating that the integration of the control surfaces limits the design flexibility as well as the possible drag reduction that can be attained. The optimised designs present an 8.4% and 13.4% increase in lift-to-drag ratio respectively compared to the initial linear lofted geometry.

The aforementioned change in the lofting technique is applied before the FFD shape optimisations are conducted and exists out of re-lofting the geometry using Gordon Surfaces to remove the undesirable characteristics of the linear lofted geometry. This lofting technique, however, introduces a thick outboard wing which results in the occurrence of shock waves on both the upper and lower surface of the wing. While the FFD optimisations reduce the shock wave strength by decreasing the wing thickness, the shocks are not eliminated due to continuity requirements related to the transition of the outboard wing to the inboard wing and winglets. These shock waves render the outboard wing rather inefficient, however as a significant increase in the lift-to-drag ratio is nonetheless obtained, it can be deduced that further design efforts to create a more efficient outboard wing will improve the aerodynamic efficiency even further.

Thence, this study has shown a successfully constrained aerodynamic shape optimisation of the outboard wing of the Flying V, however, additional research is recommended to fully exploit the potential of the aircraft. In particular, a more in-depth investigation into the possible reduction of the outboard wing thickness due to a change in the inboard wing design is required to allow for a more effective FFD optimisation. Additionally, the resulting FFD-optimised designs can be reverse-engineered to analyse them with a higher-fidelity flow model to resolve the viscous effects.

References

[1] Torenbeek, E., "Blended Wing Body and All-Wing Airliners," *European Workshop on Aircraft Design Education (EWADE)*, 2007, pp. 1–9.

[2] Smith, P., and Okonkwo, H., "Review of Evolving Trends in Blended Wing Body Aircraft Design," *Progress in Aerospace Sciences*, Vol. 82, 2016, pp. 1–23. https://doi.org/10.1016/j.paerosci.2015.12.002.

[3] Qin, N., Vavalle, A., and Moigne, A., "Spanwise Lift Distribution for Blended Wing Body Aircraft," *Journal of Aircraft*, Vol. 42, No. 2, 2005, pp. 356–365. https://doi.org/10.2514/1.4229.

[4] Qin, N., Vavalle, A., Le Moigne, A., Laban, M., Hackett, K., and Weinerfelt, P., "Aerodynamic considerations of blended wing

31

body aircraft," *Progress in Aerospace Sciences*, Vol. 40, No. 6, 2004, pp. 321–343. https://doi.org/10.1016/j.paerosci.2004.08.001.

[5] Qin, N., *Aerodynamic Studies for Blended Wing Body Aircraft*, Multidisciplinary Analysis Optimization Conferences, American Institute of Aeronautics and Astronautics, 2002, pp. 1–11. https://doi.org/10.2514/6.2002-5448.

[6] Benad, J., "The Flying V - A new Aircraft Configuration for Commercial Passenger Transport," *Deutscher Luft- und Raumfahrtkongress 2015*, 2015, pp. 1–8. https://doi.org/10.25967/370094.

[7] Smith, H., "College of Aeronautics Blended Wing Body Development Programme," *ICAS Congress*, 2000, pp. 1–10.

[8] Storck, R., *Flying Wings: Die historische Entwicklung der Nurflügelflugzeuge der Welt*, Bernard & Graefe, 2002.

[9] Lyu, Z., and Martins, J., "Aerodynamic design optimization studies of a blended-wing-body aircraft," *Journal of Aircraft*, Vol. 51, No. 5, 2014, pp. 1604–1617. https://doi.org/10.2514/1.C032491.

[10] Lee, A., Reist, T., and Zingg, D., "Further exploration of regional-class hybrid wing-body aircraft through multifidelity optimization," *AIAA Scitech 2021 Forum*, 2021, pp. 1–21. https://doi.org/10.2514/1.C034703.

[11] Staub, F., Morita, N., Entzinger, J., and Tsuchiya, T., *Aerodynamic Design Trade Study and Optimization of a Blended Wing Body Airliner*, AIAA Aviation Forum, American Institute of Aeronautics and Astronautics, 2019, pp. 1–15. https://doi.org/10.2514/6.2019-3172.

[12] Faggiono, F., "Aerodynamic Design Optimisation of a Flying V Aircraft," Thesis, University of Technology Delft, 2016.

[13] van der Pluijm, R., "Cockpit Design and Integration into the Flying V," Thesis, University of Technology Delft, 2021.

[14] Brouwer, Y., "Constrained Aerodynamic Optimization of the Flying-V Nose Cone and CenterBody Fairing," Thesis, University of Technology Delft, 2022.

[15] Horwitz, J., "Parametric Design of the Flying-V Winglets for Improved Lateral-Directional Stability and Control," Thesis, University of Technology Delft, 2021.

[16] Oosterom, W., "Flying-V Family Design," Thesis, University of Technology Delft, 2021.

[17] Hillen, M., "Parametrisation of the Flying V Outer Mould Line," Thesis, University of Technology Delft, 2020.

[18] Kulfan, B., "CST Universal Parametric Geometry Representation Method with Application to Supersonic Aircraft," *4th International Conference on Flow Dynamics*, 2006, pp. 1–35. https://doi.org/10.1017/S0001924000003614.

[19] Gordon, W., "Spline-Blended Surface Interpolation Through Curve Networks," *Journal of Mathematics and Mechanics*, Vol. 18, No. 10, 1969, pp. 931–952.

[20] Siggel, M., Pelz, M., Rusch, K., and Kleinert, J., "The TiGL Geometry Library and its Current Mathematical Challenges," *Simulation & Software Technology*, 2017.

[21] Palermo, M., and Vos, R., "Experimental Aerodynamic Analysis of a 4.6%-Scale Flying-V Subsonic Transport," *AIAA Scitech 2020 Forum*, American Institute of Aeronautics and Astronautics Inc. (AIAA), United States, 2020. https://doi.org/10.2514/6.2020-2228.

[22] Nelson, R., *Flight Stability and Automatic Control*, Aerospace series, McGraw-Hill, 1989.

[23] Storn, R., and Price, K., "Differential Evolution – A Simple and Efficient Heuristic for global Optimization over Continuous Spaces," *Journal of Global Optimization*, Vol. 11, No. 4, 1997, pp. 341–359. https://doi.org/10.1023/A:1008202821328.

[24] Drela, M., and Youngren, H., "AVL 3.26 user primer," , 2006. URL https://web.mit.edu/drela/Public/web/avl/.

[25] Palacios, F., Alonso, J., Duraisamy, K., Colonno, M., Hicken, J., Aranake, A., Campos, A., Copeland, S., Economon, T., Lonkar, A., Lukaczyk, T., and Taylor, T., *Stanford University Unstructured (SU2): An open-source integrated computational environment for multi-physics simulation and design*, Aerospace Sciences Meetings, American Institute of Aeronautics and Astronautics, 2013, pp. 1–60. https://doi.org/10.2514/6.2013-287.

[26] Ruiz Garcia, A., Brown, M., Atherstone, D., van Arnhem, N., and Vos, R., "Aerodynamic Model Identification of the Flying V from Sub-Scale Flight Test Data," *AIAA Scitech 2022 Forum*, 2022. https://doi.org/10.2514/6.2022-0713.

[27] van der Schaft, L., "Development, Model Generation and Analysis of a Flying V Structure Concept," Thesis, University of Technology Delft, 2017.

[28] Giorgi, G., and Kjeldsen, T., *Traces and Emergence of Nonlinear Programming*, 2014. https://doi.org/10.1007/978-3-0348-0439-4.

[29] Sederberg, T. W., and Parry, S. R., "Free-Form Deformation of Solid Geometric Models," Association for Computing Machinery, New York, NY, USA, 1986, p. 151–160. https://doi.org/10.1145/15922.15903.

[30] Yang, G., Da Ronch, A., Drofelnik, J., and Xie, Z., "Sensitivity assessment of optimal solution in aerodynamic design optimisation using SU2," *Aerospace Science and Technology*, Vol. 81, 2018, pp. 362–374. https://doi.org/10.1016/j.ast.2018.08.012.

[31] Dwight, R. P., "Robust Mesh Deformation using the Linear Elasticity Equations," *Computational Fluid Dynamics 2006*, edited by H. Deconinck and E. Dick, Springer Berlin Heidelberg, Berlin, Heidelberg, 2009, pp. 401–406. https://doi.org/10.1007/978-3-540-92779-2_62.

[32] Roysdon, P., "Blended wing body lateral-directional stability investigation using 6DOF simulation," *Proceedings of the Institution of Mechanical Engineers, Part G: Journal of Aerospace Engineering*, Vol. 228, No. 1, 2014, pp. 7–19. https://doi.org/10.1177/0954410013483633.

[33] Wang, K., and Zhou, Z., "Aerodynamic Design, Analysis and Validation of a Small Blended-Wing-Body Unmanned Aerial Vehicle," *Aerospace*, Vol. 9, No. 1, 2022. https://doi.org/10.3390/aerospace9010036.

[34] Palermo, M., "The Longitudinal Static Stability and Control Characteristics of a Flying V Scaled Model: An Experimental and Numerical Investigation," Thesis, University of Technology Delft, 2019.

[35] Ruiz Garcia, A., "Aerodynamic Model Identification of the Flying V using Wind Tunnel Data," Thesis, University of Technology Delft, 2019.

[36] Viet, R., "Analysis of the flight characteristics of a highly swept cranked flying wing by means of an experimental test," Thesis, University of Technology Delft, 2019.

[37] Gur, O., Mason, W. H., and Schetz, J. A., "Full-Configuration Drag Estimation," *Journal of Aircraft*, Vol. 47, No. 4, 2010, pp. 1356–1367. https://doi.org/10.2514/1.47557.

[38] Raymer, D., *Aircraft Design: A Conceptual Approach*, Sixt Edition, American Institute of Aeronautics and Astronautics, 2018.

[39] Chan, W., Gomez, R., Rogers, S., and Buning, P., "Best Practices in Overset Grid Generation," *32nd AIAA Fluid Dynamics Conference and Exhibit*, 2002. https://doi.org/10.2514/6.2002-3191.

[40] Kurowski, P., and of Automotive Engineers, S., *Finite Element Analysis for Design Engineers*, Electronic publications, SAE International, 2017.

[41] Gokhale, N., *Practical Finite Element Analysis*, Finite To Infinite, 2008.

[42] Schmitt, C. F., V, "Pressure Distributions on the Onera-M6-Wing at Transonic Mach Numbers: Experimental Data Base for Computer Program Assessment," Tech. report 138, Fluid Dynamics Working Group 04, AGARD AR, 1979.

[43] Blazek, J., *Computational Fluid Dynamics: Principles and Applications*, Elsevier, 2005.

[44] Menter, F., "Two-equation eddy-viscosity turbulence models for engineering applications," *AIAA Journal*, Vol. 32, 1994, pp. 1598–1605. https://doi.org/10.2514/3.12149.

[45] Araya, G., "Turbulence Model Assessment in Compressible Flows around Complex Geometries with Unstructured Grids," *Fluids*, Vol. 4, 2019, p. 81. https://doi.org/10.3390/fluids4020081.

[46] Moigne, A. L., and Qin, N., "Variable-Fidelity Aerodynamic Optimization for Turbulent Flows Using a Discrete Adjoint Formulation," *AIAA Journal*, Vol. 42, No. 7, 2004, pp. 1281–1292. https://doi.org/10.2514/1.2109.

[47] Nielsen, E. J., and Anderson, W. K., "Recent Improvements in Aerodynamic Design Optimization on Unstructured Meshes," *AIAA Journal*, Vol. 40, No. 6, 2002, pp. 1155–1163. https://doi.org/10.2514/2.1765.

[48] Crovato, A., Almeida, H. S., Vio, G., Silva, G. H., Prado, A. P., Breviglieri, C., Guner, H., Cabral, P. H., Boman, R., Terrapon, V. E., and Dimitriadis, G., "Effect of Levels of Fidelity on Steady Aerodynamic and Static Aeroelastic Computations," *Aerospace*, Vol. 7, No. 4, 2020. https://doi.org/10.3390/aerospace7040042.

33

[49] Anderson, J. D., *Fundamentals of aerodynamics*, 5th ed., McGraw-Hill, 2011.

[50] Ma, L., Lu, L., Fang, J., and Wang, Q., "A study on turbulence transportation and modification of Spalart–Allmaras model for shock-wave/turbulent boundary layer interaction flow," *Chinese Journal of Aeronautics*, Vol. 27, No. 2, 2014, pp. 200–209. https://doi.org/10.1016/j.cja.2014.02.008.

[51] Lyu, Z., and Martins, J. R. R. A., "Aerodynamic design optimization studies of a blended-wing-body aircraft," *Journal of Aircraft*, Vol. 51, No. 5, 2014, pp. 1604–1617. https://doi.org/10.2514/1.C032491.

[52] Lyu, Z., Kenway, G. K., and Martins, J. R., "Aerodynamic shape optimization investigations of the common research model wing benchmark," *AIAA Journal*, Vol. 53, No. 4, 2015, p. 968 – 985. https://doi.org/10.2514/1.J053318.

[53] Yu, Y., Lyu, Z., Xu, Z., and Martins, J. R. R. A., "On the influence of optimization algorithm and initial design on wing aerodynamic shape optimization," *Aerospace Science and Technology*, Vol. 75, 2018, pp. 183–199. https://doi.org/10.1016/j.ast.2018.01.016.

[54] Oosterom, W., and Vos, R., *Conceptual Design of a Flying-V Aircraft Family*, 2022. https://doi.org/10.2514/6.2022-3200.

[55] Palacios, F., Economon, T., Aranake, A., Copeland, S., Lonkar, A., Lukaczyk, T., Manosalvas-Kjono, D., Naik, K., Padrón, A., Tracey, B., Variyar, A., and Alonso, J., "Stanford University Unstructured (SU2): Analysis and Design Technology for Turbulent Flows," 2014. https://doi.org/10.2514/6.2014-0243.